

# Inertial Confinement Fusion Annual Report

October 1, 2003 through September 30, 2004



Cryoholraum

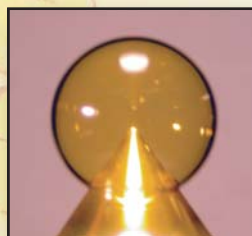


Double Shell Fixture

## Micromachined Components

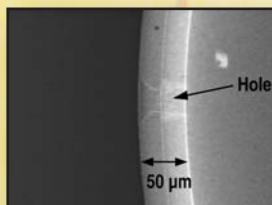


Double Shell Target



Fast Ignition Target

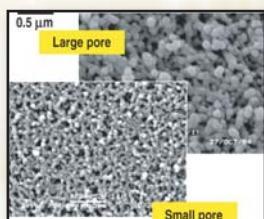
## Targets



Hole  
50 μm



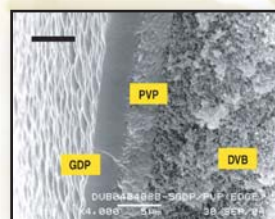
## Beryllium Capsules



RF Aerogel Foam

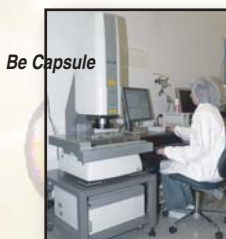


DVB Shells



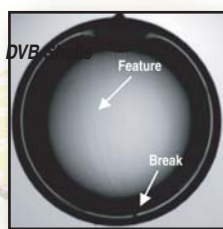
Coated DVB

## Foam Capsules



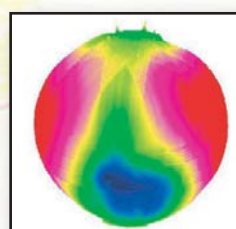
Be Capsule

Automated Microscope



DVB

Capsule Cryolayer Analysis



Capsule Spheremap

## Characterization

## DISCLAIMER

This report was prepared as an account of work sponsored by an agency of the United States Government. Neither the United States Government nor any agency thereof, nor any of their employees, makes any warranty, express or implied, or assumes any legal liability or responsibility for the accuracy, completeness, or usefulness of any information, apparatus, product, or process disclosed, or represents that its use would not infringe privately owned rights. Reference herein to any specific commercial product, process, or service by trade name, trademark, manufacturer, or otherwise, does not necessarily constitute or imply its endorsement, recommendation, or favoring by the United States Government or any agency thereof. The views and opinions of authors expressed herein do not necessarily state or reflect those of the United States Government or any agency thereof.

GA-A24975

**INERTIAL CONFINEMENT FUSION  
TARGET COMPONENT FABRICATION AND  
TECHNOLOGY DEVELOPMENT SUPPORT**

**ANNUAL REPORT TO THE  
U.S. DEPARTMENT OF ENERGY**

**OCTOBER 1, 2003 THROUGH SEPTEMBER 30, 2004**

**by  
PROJECT STAFF**

**Work prepared under  
Department of Energy  
Contract No. DE-AC03-01SF22260**

**GENERAL ATOMICS PROJECT 30095  
DATE PUBLISHED: DECEMBER 2005**





## EXECUTIVE SUMMARY

This report documents fiscal year 2004 activity on the U.S. Department of Energy (DOE) National Nuclear Security Administration (NNSA) task order contract for Inertial Confinement Fusion (ICF) Target Component Fabrication and Technology Development Support with General Atomics (GA) and partner/subcontractor Schafer Corporation. Work performed spans development, production, and engineering of planar and spherical targets, target components, and cryogenic systems for the NNSA ICF Laboratories: Lawrence Livermore National Laboratory (LLNL); Los Alamos National Laboratory (LANL); Sandia National Laboratory (SNL); the University of Rochester Laboratory for Laser Energetics (UR/LLE); and the Naval Research Laboratory (NRL) in Washington, D.C.

For more than ten years, the GA/Schafer Inertial Confinement Technology team has partnered with the NNSA ICF Laboratories developing and providing targets and related technologies for ongoing and future driver target interaction laboratory experiments. The team expertise is broad with interests and capabilities in all of the relevant areas of polymer and metal component fabrication, gas filling (including tritium), machining, characterization, and handling as diagrammed in Fig. E-1.

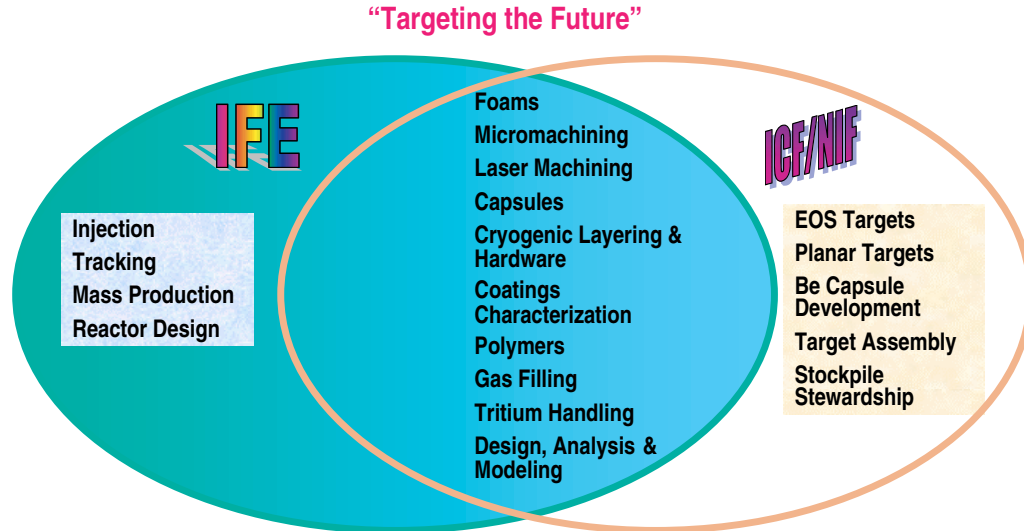


Fig. E-1. The GA/Schafer Inertial Confinement Technology team expertise supports the NNSA national security missions as well as derivative missions such as Inertial Fusion Energy (IFE).

Highlights of the GA/Schafer ICF technology work performed under DOE Contract No. DE-AC03-01SF22260 in FY03 comprise the subject of this report. Comments and requests for further information may be directed to the GA Inertial Fusion Technology Program Manager, Joe.Kilkenny@gat.com, (858) 455-3571.



## ACRONYMS

AFM	atomic force microscope
CDR	Conceptual Design Report
CPL	cryogenic pressure loader
CRF	carbonized resorcinol formaldehyde
CTM	cryogenic target mount
CW	continuous wave
D <sub>2</sub> TS	deuterium test system
D-GDP	deuterated polymer
DT	deuterium-tritium
DTRA	Defense Threat Reduction Agency
DVB	divinylbenzene
EDAX	energy dispersive x-ray analysis
EOS	equation of state
FI	fast ignition
GFY	government fiscal year
GA	General Atomics
GDP	glow discharge polymer
H-L	half-life
HD	hydrogen deuteride
HEDP	high energy density plasma
I-TIC	ignition-target inserter and cryostat
ICF	Inertial Confinement Fusion
IDL™	Interactive Data Language
IFE	Inertial Fusion Energy
IFT	Inertial Fusion Technology
ILE	Institute of Laser Engineering, Japan
IPA	isopropanol
IR	infrared

LANL	Los Alamos National Laboratory
LEH	laser entrance hole
LLNL	Lawrence Livermore National Laboratory
NCTS	NIF Cryogenic Target System
NIF	National Ignition Facility
NNSA	National Nuclear Security Administration
NRL	Naval Research Laboratory
PAMS	poly- $\alpha$ -methylstyrene
PCHMS	polycyclohexyl-methylsilylene C <sub>7</sub> H <sub>14</sub> Si
PV	peak-to-valley
PVA	polyvinyl alcohol
PVP	polyvinylphenol
rf	radio frequency
RF	resorcinol formaldehyde
RT	Rayleigh-Taylor
SEM	scanning electron microscopy
Si-GDP	silicon-doped glow discharge polymer
SM	spheremapper
SM/WM	spheremapper/wallmapper
SNL	Sandia National Laboratory
TARPOS	TARget POSitioner
TGA	thermogravimetric analysis
TIC	target insertion cryostat
TMG	tetramethyl germanium
TPX	commercial designation of the polymer produced by the polymerization of 4-methylpentene-1
UR/LLE	University of Rochester Laboratory for Laser Energetics
UV	ultraviolet
WBS	work breakdown structure
WETF	Weapons Engineering Tritium Facility
WM	wallmapper
XRF	x-ray fluorescence

## TABLE OF CONTENTS

<b>EXECUTIVE SUMMARY .....</b>	<b>iii</b>
<b>1. INTRODUCTION .....</b>	<b>1</b>
<b>2. 04LL02 LLNL MICROMACHINED TARGET COMPONENTS (J. KAAE) .....</b>	<b>3</b>
<b>3. 04LL03 COMPOSITE POLYMER CAPSULES (D. STEINMAN) .....</b>	<b>5</b>
<b>4. 04LA01 ON-SITE SUPPORT AT LANL (K. SHILLITO) .....</b>	<b>9</b>
<b>5. 04LA02 LANL GLASS AND POLYMER CAPSULES (D. STEINMAN) .....</b>	<b>11</b>
<b>6. 04LA03 FOAM SUPPORT (K. SHILLITO) .....</b>	<b>15</b>
<b>7. 04LA04 MICROMACHINED TARGET COMPONENTS FOR LANL (J. KAAE) .....</b>	<b>17</b>
<b>8. 04NR01 NRL TARGET DELIVERIES (T. WALSH) .....</b>	<b>19</b>
<b>9. 04SL01 TARGET COMPONENTS AND CAPSULES (D. STEINMAN, J. KAAE) .....</b>	<b>23</b>
9.1. Micromachined Components .....	23
9.2. SNL Capsule Production .....	24
<b>10. 04SL02 TARGET FABRICATION (D. SHROEN) .....</b>	<b>27</b>
<b>11. 04UR01 TARGET PRODUCTION AND DELIVERY (A. NIKROO) .....</b>	<b>31</b>
11.1. Center for Coatings, Polymer and Foam Shell Development .....	31
11.1.1. Introduction .....	31
11.1.2. UR/LLE Deliveries .....	31
<b>12. 04UR02 CRYOGENIC CAPSULE DEVELOPMENT (A. NIKROO) .....</b>	<b>35</b>
12.1. Foam Shell Fabrication .....	35
<b>13. 04CR/LA1 CRYOCONDENSATION APPARATUS FOR BERYLLIUM CAPSULES (N. ALEXANDER) .....</b>	<b>43</b>

**14. 04CR/LL1 ENHANCED CRYO TARGET FIELDING DEVELOPMENT (D. BITTNER) ..... 45**

    14.1. Slow Cooldown Experiments under Low IR Power ..... 45

    14.2. Modeling of Cracks in Ice Layers ..... 45

**15. 04CR/NCTS NIF CRYO TARGET SYSTEM DEVELOPMENT AND ENGINEERING (N. ALEXANDER) ..... 49**

**16. 04NIF/CD NIF CAPSULE DEVELOPMENT (A. NIKROO) ..... 55**

    16.1. NIF/CD Evaluation of Ge-doped CH/CD Ablator ..... 55

        16.1.1. Fabrication Technique ..... 55

        16.1.2. Surface Finish ..... 56

**17. 04CAP-1 CAPABILITIES IMPROVEMENT (A. NIKROO) ..... 61**

    17.1. Glass Permeation Barrier Target Fabrication and Characterization ..... 61

    17.2. 3D Surface Reconstruction of ICF Shells after Full Surface Spheremapping ..... 62

    17.3. In-situ Ultrasonic Witness Plate Measurements ..... 64

**18. 04PR01 PRECISION RADIOGRAPH (R. STEPHENS) ..... 67**

**19. 04SL03 BERYLLIUM SHELLS FOR SNL (A. NIKROO) ..... 71**

**20. 04EQ-1 HIGH PRECISION MILLING MACHINE (J. KAAE) ..... 75**

**21. 04EQ-2 PURCHASE AND ASSEMBLE FILM MAPPING SYSTEM (K. SHILLITO) ..... 77**

**22. 04EQU-3 DIAMOND TURNING MACHINE (J. KAAE) ..... 79**

**23. 04EQU-4 SURFACE PROFILER (K. SHILLITO) ..... 81**

**24. 04EQU-5 AUTOMATED INSPECTION MICROSCOPE (K. SHILLITO) ... 83**

**25. PUBLICATIONS ..... 85**

**LIST OF FIGURES**

1-1. The GA/Schafer Inertial Confinement Technology team ..... iii

2-1. One half of a cryohohlraum ..... 3

2-2. Small gold cups of a range of sizes sitting on a penny ..... 4

2-3. Epoxy cylinders designed to contain gas ..... 4

2-4.	A thin-walled gold hohlraum sitting on a dime .....	4
3-1.	In FY04, we fabricated and assembled double-shell targets for LLNL .....	5
3-2.	Another double-shell target we fabricated for LLNL was a silver-coated glass shell .....	6
3-3.	Temperature is the key to fabricating Hoppe shells with short H-Ls .....	7
3-4.	A 400 $\mu\text{m}$ diameter Hoppe glass shell .....	7
5-1.	Scanning electron microscopy image of $\sim 7 \mu\text{m}$ thick iron coating .....	12
5-2.	SEM images of chromium layer deposited on PAMS shell .....	12
5-3.	SEM image of wall cross-section of chromium coated PAMS shell .....	12
5-4.	We expanded the capabilities of our sphere/wallmapper system .....	13
6-1.	Silica aerogel reactor .....	15
7-1.	Photomicrograph of aluminum band electroplated on copper mandrel .....	17
8-1.	FY04 target mix .....	19
8-2.	Filmetric film mapper .....	22
8-3.	NexIV automated measure scope .....	22
8-4.	Ambios stylus surface profile .....	22
9-1.	Gold hohlraum on the copper mandrel .....	23
9-2.	Gold hohlraum on the copper mandrels, which will be dissolved out .....	23
9-3.	A complex copper fixture to be used in cryogenic double-shell tests .....	24
9-4.	A very thin aluminum foil .....	24
9-5.	A gold fiducial ring with thin spacing extensions .....	24
9-6.	X-radiograph of 2 mm SNL capsule .....	25
9-7.	X-ray image of a $\sim 50 \mu\text{m}$ walled SNL capsule .....	25
9-8.	Capsule wall thickness plot .....	26
10-1.	Graph of parts processed per month .....	27
10-2.	An end on view of the capsule in the secondary hohlraum .....	28
10-3.	Schematic of the fast ignitor target design .....	28
10-4.	A radiographic image of a shaped foam .....	29
11-1.	We continued our responsive, on time target deliveries to LLE .....	32
11-2.	The various types of capsules delivered .....	32
12-1.	Plot of NC versus delta density .....	36
12-2.	Foam-filled cylinders became an often requested target in FY04 .....	36
12-3.	Gapless foam-full density multi-layers flats were developed in FY04 .....	37

12-4. Photo of a completed target shot at OMEGA ..... 37

12-5. White light interferometer 3D profile of the target ..... 37

12-6. Electron microscope images of standard pore RF foam ..... 38

12-7. Photo of RF shells made using standard pore RF and large pore RF ..... 38

12-8. Large batch of DVB shells ..... 39

12-9. Cross-sectional electron microscope image of a PVP + GDP coated DVB shell ..... 39

12-10. Using the PAMS/GDP technique to make monolithic fill tubes ..... 40

12-11. Closed end fill tube surrogate ..... 40

13-1. A thermal model indicates that the window will be warm enough to prevent condensation ..... 43

13-2. The cryocondensation cryostat uses a second outer copper spring ..... 44

13-3. The top level assembly drawing for the cryocondensation cryostat ..... 44

14-1. Plot of the rms versus temperature for the slow cooldown of a solid deuterium layer under IR illumination ..... 45

14-2. An image of an ice layer with a break in the brightband ..... 46

14-3. Raytrace image of an ice layer ..... 46

15-1. Axial one-sided shroud retraction concept ..... 49

15-2. This concept allows the cryocooler to be turned off before the shot ..... 51

15-3. Models were made of concepts of many NCTS systems ..... 51

15-4. The cryocondensation “drill, fill, and plug” concept uses cryogenic temperatures ..... 52

15-5. Thermal model indicates that the capsule can be cooled ..... 53

15-6. Apparatus for testing capsule to cone seal down to 77 K ..... 53

15-7. Apparatus for testing capsule to cone seal at 10 to 20 K ..... 54

15-8. Concept for a miniature see-through vial to replace capsule ..... 54

16-1. Full thickness CH shells very nearly meeting the “NIF standard” ..... 56

16-2. The surface height deviation as a function of angle ..... 57

16-3. Examples of AFM power spectra of full thickness pure CH shells ..... 59

16-4. “Full spheremap” of one of the shells ..... 59

17-1. Three spheremapper traces 40  $\mu\text{m}$  apart near the equator of a NIF-sized shell .. 62

17-2. 3D visualization of the process flow steps with all distortions magnified 300x . 63

17-3. PAMS shell surface reconstructed to 5 nm accuracy ..... 64

18-1. Scaled counts as a function of shaft angle ..... 68

18-2.	Deviation from fit for the two runs with more than $10^{10}$ counts/angle .....	69
19-1.	SEM image of a $\sim 50 \mu\text{m}$ Be layer microstructure change with deposition rate .	71
19-2.	Pressure cell with orthogonal optical access .....	72
19-3.	Excimer laser drilled hole in CH mandrel .....	72
19-4.	Dycor System 200 .....	72
19-5.	Hole drilled in CH mandrel is duplicated in Be coating .....	73
20-1.	Kern high-precision milling machine .....	75
21-1.	Filmetrics F50 Film Mapper .....	77
22-1.	Nanotech 220UPL-HD diamond turning machine .....	79
23-1.	Ambios XP-2 profilometer .....	81
24-1.	A Nikon NEXIV VMR 3020 Video Measuring System .....	83

## LIST OF TABLES

2-1.	Micromachined target components produced for LANL .....	3
3-1.	Orders processed for LLNL .....	5
5-1.	LANL FY04 task orders .....	11
7-1.	Micromachined target components produced for LANL .....	17
8-1.	List of the patterned substrates currently available at Schafer for casting .....	20
8-2.	Schafer Livermore foam systems .....	21
9-1.	Micromachined target components produced for SNL .....	23
9-2.	SNL FY04 capsule deliveries .....	25
11-1.	LLE target deliveries in FY04 .....	32



## 1. INTRODUCTION

Inertial Confinement Fusion (ICF) is a research and development activity supported under the auspices of the U.S. Department of Energy (DOE) National Nuclear Security Administration (NNSA). One goal of the ICF program is controlled laboratory implosion of fusionable material to a condition of ignition and propagating burn.

ICF relies on inertia to confine fusionable material, usually a mixture of deuterium and tritium (DT), for the time required to create a fusion reaction. Matter, which reaches this inertially confined state by means of compression from lasers or x-rays, can be considered to be a high energy density plasma (HEDP) for essentially all phases of the process from earliest compression through energy production through replete, extinguishing burn.

The canonical implosion scenario is that of central hot spot ignition in which a hollow, impermeable DT sphere is symmetrically imploded to a density ( $\rho$ ), radius ( $R$ ) product of 0.3 g/cc and a temperature ( $T$ ) of order 10 keV. In the limit of radial symmetry, success (propagating burn) is predicted for a wide range of driver-capsule configurations.

The two most commonly envisioned central hot spot systems are direct and indirect drive ICF. In direct drive, the driving beams, usually high intensity lasers (many  $\times 10^{14}$  W/cm<sup>2</sup>) of short wavelength light (0.33  $\mu$ m) directly irradiate a spherical capsule surface. As the surface is heated, matter boils off and the capsule implodes. For shaped pulse driving beams, in which the intensity is controlled so as to drive well-timed shocks in the shell and accelerate the compressed hollow sphere walls inward to high final velocities ( $3 \times 10^7$  cm/s), a design space has been found where fusion conditions are predicted to occur. For indirect drive, the process is similar, with laser light replaced by a spatially uniform bath of x-rays (wavelength  $\sim 0.01$   $\mu$ m). The x-rays are produced and contained in a spherical or cylindrical can, a hohlraum, that is fabricated of metals of high atomic number. NNSA drivers used to generate the hohlraum x-rays include lasers and z-pinches.

It is generally agreed that five criteria determine a successful ICF implosion, each with outstanding issues and active research. First, a sufficient amount of driver energy must be transferred to the shell. Plasma instabilities in the shell corona can inhibit successful coupling of driver energy into the target. This continues to be an area of ongoing research with regimes identified that minimize plasma instabilities and allow for up to 80% driver energy absorption. Second, the capsule must be imploded on a sufficiently low adiabat for fusion conditions to be achievable with laboratory-scale drivers. Adverse preheat mechanisms include shock mistimings (5% or greater), radiation effects, and mixing from very short wavelength instabilities. Considerable research in equation of state (EOS) and opacity results from this criterion. Third, the implosion must be sufficiently symmetric at length scales long relative to the shell thicknesses for the generation of a well-formed hot spot. This criterion, which sets a shell uniformity requirement of a few percent and also limits time independent

drive asymmetry at long perturbation wavelengths ( $l < 32$ ) to a few percent, is achievable with existing technologies. Fourth, the shell must be sufficiently stable to the short wavelength Rayleigh-Taylor (RT) instability to confine the core gas to full implosion in order for ignition conditions to be achieved. This instability, which is seeded by all of the small-scale imperfections of real-world driving beams and shell surface and mass, is the subject of intense ongoing research. Because the RT instability is vortical in nature, mitigation is sought primarily in a tailoring of the ICF pellet gradients to reduce the vorticity source term (a function of the cross product of gradients of  $\rho$  and  $T$ ) at both the outer and inner shell surfaces and to increasing the ablation velocity at the shell surfaces in order to pull away as much as possible the vorticity generated. Fifth, the pellet must reach a condition of sufficient  $\rho R$  and  $T$  for alpha-particle-driven ignition and propagating burn to occur.

As with many systems with well-defined postulates, the relaxation of one criterion can sometimes lead to the most interesting alternate systems. A classic example is the birth of complex variable theory which came about when parallel lines were allowed to meet at infinity in an otherwise Euclidean space. In the case of ICF, relaxing completely the fourth criterion has led to the idea of fast ignition (FI). In FI, the  $\rho R$  for ignition is first achieved with standard drivers and capsules that range from spherical shells to hemispheres of webbed foams. The ignition beam is then envisioned to be generated from high intensity, collimated electrons or ions that result from petawatt laser matter interaction. While compression is relatively easy and has, to some level, already been demonstrated in the laboratory, coupling the ignitor “match” to the compressed fuel is far from determined. The introduction of this concept in the early 1990s, along with the development of very high intensity (order  $10^{19}$  W/cm<sup>2</sup> or higher) laser drivers, has resulted in significant active research in very high intensity laser matter and laser plasma interactions.

The GA/Schafer team fabricates components and complete target assemblies for the NNSA ICF laboratories (Lawrence Livermore National Laboratory, Los Alamos National Laboratory, Sandia National Laboratory, the University of Rochester Laboratory for Laser Energetics, and the Naval Research Laboratory) to address a wide range of experimental criteria that are relevant to ICF and HEDP physics. These components include: gasbags for plasma instability studies, doped planar and shaped targets for radiation preheat and shock timing investigations, well-characterized spheres with a variety of gas fills for low-mode asymmetry studies under a range of conditions, targets that enable investigation of the Richtmyer-Meshkov and RT instabilities, and we are assisting in the development of National Ignition Facility (NIF) ignition targets and cryogenic systems.

The work of target and target component fabrication is fundamentally cross-disciplinary in nature. Most new target types and developments are research results from proactive teams of chemists, material scientists, physicists, and characterization and fabrication engineers, who, together, produce new target systems and capabilities.

## 2. 04LL02 LLNL MICROMACHINED TARGET COMPONENTS (J. KAAE)

In FY04, we produced 741 micromachined target components for LLNL. These were made up of many different types. They are listed in Table 2-1.

**Table 2-1**  
**Micromachined Target Components Produced for LANL**

<b>Component</b>	<b>Different Designs</b>	<b>Total No.</b>
Conventional Au Hohlräume	21	291
Au Cryo hohlraums	1	22
Au Trapezoidal Shields	1	30
Polyimide Sine Wave Plates	1	1
Al Mandrels for Cocktail Coating	1	62
Small Au Cups	10	67
Epoxy Washers	2	28
Epoxy Gas Bags	2	28
Al Witness Plates	1	22
Au Cylinders	3	31
PERT Targets (Br-doped CH plates)	11	54
Au Cones	2	16
Half-round Au Cylinders	1	19
Epoxy Hohlräume	1	24
Roughened Au Disks	1	4
Polystyrene Spacers	1	13
Thin-walled Au Hohlräume	5	20
Au Hohlräume with SiO <sub>2</sub> Liners	1	9

Thus, we seldom worked on one type of component for very long. The target component task required us to constantly adapt from production of one type of component to another.

Photographs of some of the components are shown in Figs. 2-1 through 2-4.



Fig. 2-1. One half of a cryohohlraum. These components are produced in halves and are joined once the capsule is mounted. The inner barrel has been roughened to scatter infrared (IR) radiation, which is used to aid layering of the DT ice in the capsule.



Fig. 2-2. Small gold cups of a range of sizes sitting on a penny. Note the very small cups within the zeros of the date.



Fig. 2-3. Epoxy cylinders designed to contain gas. They are sitting on a penny. A membrane will be mounted on the flange at the end of each cylinder.



Fig. 2-4. A thin-walled gold hohlraum sitting on a dime. The Au wall of the hohlraum is  $2\ \mu\text{m}$  thick and is reinforced with a  $100\ \mu\text{m}$  thick layer of epoxy.

### 3. 04LL03 COMPOSITE POLYMER CAPSULES (D. STEINMAN)

Task Leader: D.A. Steinman

Capsule production for LLNL in FY04 saw an increase in target numbers and complexity. The Table 3-1 lists the orders processed for LLNL under the ICF contract:

**Table 3-1**  
**Orders Processed for LLNL**

Target Type	Orders	Capsules
Double-shell targets	6	18
Hoppe glass shells	8	59
CH Hemi-shells	1	20
500 mm CH capsules	9	121
900 mm CH capsules	5	55
2 mm × 12 mm GDP shells for NIF Be capsules	4	333
Total	33	606

In FY04, the cost per target escalated as LLNL requested more complex targets that required micromachining, precise assembly and characterization (Figs. 3-1 and 3-2). For example, the cost per double-shell target was on the order of a hundred-fold that of the cost of a single layer, free-standing glow discharge polymer (GDP) shell.

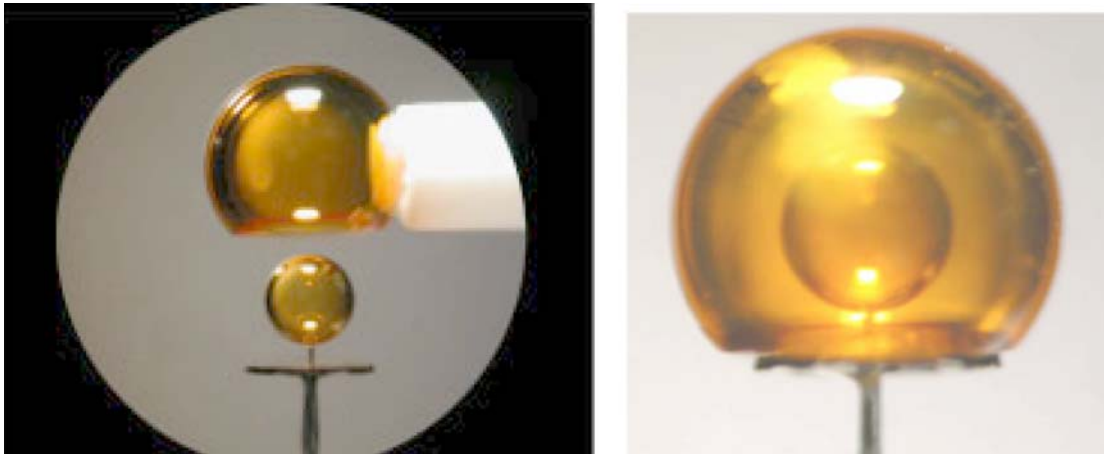


Fig. 3-1. In FY04, we fabricated and assembled double-shell targets for LLNL such as this  $580 \times 42 \mu\text{m}$  Ge-GDP inner shell mounted in a  $1270 \times 133 \mu\text{m}$  undoped-GDP outer shell with beryllium plug and filled with 1 atm nitrogen.

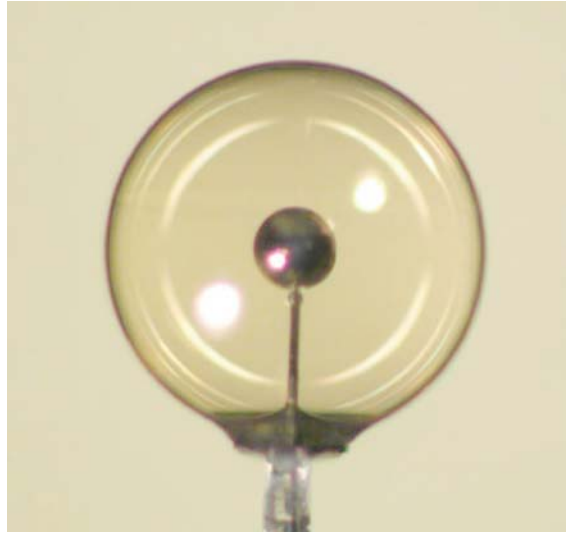


Fig. 3-2. Another double-shell target we fabricated for LLNL was a silver-coated glass shell filled with 10 atm deuterium in a CH outer shell filled with 1.5 atm xenon.

The fabrication of Hoppe shells (glass shells made by oxidizing Si-doped GDP shells) having tailored gas fill permeation characteristics was a new capability we developed under the LLNL capsule production task in FY04. The need for such capsules arose due to target fielding considerations. An LLNL order of Hoppe glass shells for use in double-shell targets was fully characterized and found to have a deuterium fill half-life (H-L) of  $\sim 11$  days. This H-L was too short for the option of filling the capsule before mounting it in the double shell, too much deuterium would out-permeate in the time required to assemble all the targets for the campaign. However, the 11 day H-L was too long for the option of assembling the double-shells then filling them at room temperature. About two months would be required to reach fill equilibrium. A solution to this problem was to make Hoppe shells with deuterium H-Ls of 1-3 days, that could be filled after assembly and brought out of the fill just prior to shot time.

We fabricated the requested short H-L capsules using the controlled atmosphere pyrolysis oven we designed and brought on line in FY03. The key to fabricating the capsules was to control the glass densification by reducing the sintering temperature. Rather than fully densifying the shells at  $\sim 1000^{\circ}\text{C}$ , using our standard procedure, we limited the temperature to  $\sim 650^{\circ}\text{C}$ . The reduced density of the glass wall resulted in shells having the desired three day deuterium H-L. The oven temperature profile depicted in Fig. 3-3 illustrates the affect of sintering conditions on Hoppe shells.

Under the LLNL capsule production task, we also were asked to develop Hoppe glass shells containing minimal amounts of residual gases. This we did by performing experiments to find optimal sintering conditions in our controlled atmosphere oven. Progress on this task required that we find a means of measuring the quantity of residual gas in the capsules. Figure 3-4 illustrates how we did this and shows our progress to date. We determined the residual gas pressure in the pictured Hoppe glass shell by immersing the shell in glycerol and

breaking it. The glycerol captures the entrapped residual gas as a spherical bubble. We measure the diameter of the bubble and calculate the volume of the residual gas that had been contained in the shell. To date, we have produced Hoppe glass shells containing as little as 0.03 atm of residual gases, primarily consisting of CO<sub>2</sub>.

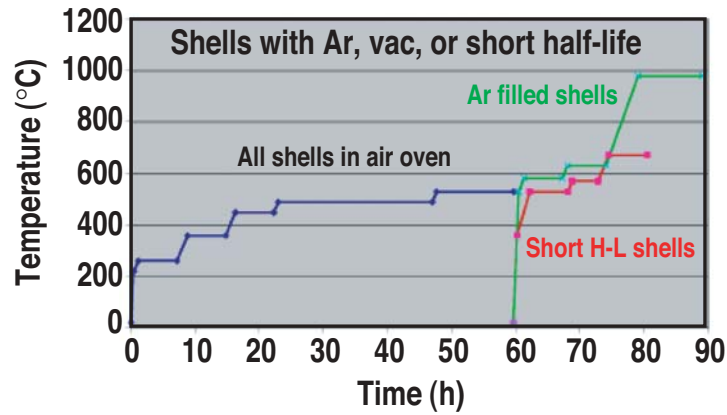


Fig. 3-3. Temperature is the key to fabricating Hoppe shells with short H-Ls. For all types of Hoppe shells, carbon and hydrogen are first oxidized away in an open air oven. Then, our controlled atmosphere oven is used at ~1000°C to make fully dense shells containing argon (or other diagnostic gases) or less than fully dense shells with short H-Ls at lower temperatures as illustrated above.

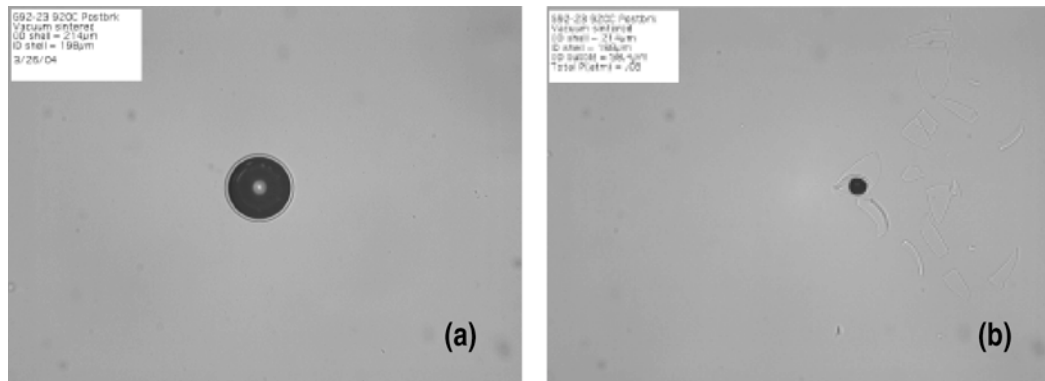


Fig. 3-4. (a) A 400 μm diameter Hoppe glass shell immersed in liquid (glycerol). (b) The broken shell shards and the bubble of residual gas (0.03 atm) that was entrapped in the shell.



#### 4. 04LA01 ON-SITE SUPPORT AT LANL (K. SHILLITO)

Task Leader: Keith Shillito

Technicians: Ron Perea

##### **Target Fabrication**

This task required the services of one full-time Q-cleared person on-site at LANL to perform micro machining, characterization and assembly of LANL targets for TRIDENT, and OMEGA. The assigned individual, Ron Perea, followed all LANL protocols regarding safe work and target documentation and delivery while reporting to a LANL scientist (Bob Day) for supervision.

Ron assembled about 150 targets per month of various sizes and shapes, consisting of gold cones with manganese or titanium inserts and fiducials, flyer plates, short pulse targets, disks of various sizes, targets with back lighters, and edge targets with backlighters. At appropriate times he assumed the Project Leader position (for Art Nobile) in charge of scheduling, ensuring finished product completion and in correct working order in a timely manner. He attended all Trident meetings with group leaders and team leaders to determine the order of shots and experiments, as well as offering presentations to the physics groups regarding capabilities at MST-7, providing updates for target fabrication for experimenters.

Throughout the year Ron supported the team leader (Bob Day) as the person in charge (PIC) when parts needed to be fabricated by the assembly team, machine shop, or the polymer group. This job involved talking to the different team leaders in an effort to coordinate schedules to get parts out in time for assembly of finished and deliverable targets.

He acted as the lead technician investigator, responsible for three or more programs with multiple interfaces. Perea worked independently and provided successful efforts to develop programs with the Trident experimenters.

Perea participated in multiple co-authorships of reports, publications, and technical society presentations detailing the assembly aspects of everything that occurs for the preparation of experimenters' talks and publications.

The work provided by GA/Schafer has required world class skills, knowledge, and abilities (cutting edge, leading development) to complete tasks, often requiring training via workshops and taking trips to learn about new developments available in the workplace. Perea proved to be a strong mentoring/supervising influence for several (>2) new LANL employees. There were many other services provided including the responsibility for safety (preparing for IWD, analysis and mitigation of hazards) for multiple complex operations. Extensive training was required (e.g. Laser operator, waste generator) in addition to the need to focus on extensive compliance issues.



## 5. 04LA02 LANL GLASS AND POLYMER CAPSULES (D. STEINMAN)

Center head: David Steinman (GA)

Technical Group

Leads: Martin Hoppe (GA), Donald Czechowicz (GA)

Scientists: Salvacion Paguio (GA) and Dale Hill (GA)

Technician: Stephen Grant (GA)

Deliveries Group

Lead: Annette Greenwood (GA)

Scientists: Jane Gibson and Melissa Kittelson (GA)

Technician: Ron Andrews (GA)

Our support for Task 04LA02 consisted of delivering capsules for LANL experiments and developing additional capsule fabrication and characterization capabilities. Specifically, we developed iron and chromium capsule coatings and the capability to sphere/wallmap shells 200  $\mu\text{m}$  in diameter. The Table 5-1 lists the task orders processed for LANL in FY04.

**Table 5-1**  
**LANL FY04 Task Orders**

Target Type	Orders	Capsules
Hoppe glass shells (1100 x 4 $\mu\text{m}$ )	1	22
Fe and Cr on PAMS shells or sapphire beads	2	10
Cr on 0.5 mm CH shells	1	10
0.5 mm CH composite shells	1	22
Multi-layer CH capsules	<u>5</u>	<u>33</u>
Total	10	97

Coating of iron onto sapphire ( $\text{Al}_2\text{O}_3$ ) balls was developed using our DC magnetron sputtering unit. Due to the magnetic field strength limit of our gun, we could only use a 0.030 in. thick Fe sputtering target. This limited our coating thickness of each sputter target to  $\sim 2.5 \mu\text{m}$ . Under our operating conditions, which were 10 mTorr Ar and 100 W DC power, each target of 0.030 in. thickness only lasted  $\sim 4$  h. Therefore, it was necessary to change the target in the middle of the run to achieve thicker coatings.

We tested two kinds of coating techniques, rolling and bouncing the balls during the coating run. Due to static attraction of the balls, we gave up on rolling and used bouncing as the means of coating them. With the sapphire balls 6 in. away from the sputtering target the average coating rate was 0.6  $\mu\text{m}/\text{h}$ . Figure 5-1 shows an iron coated sapphire ball whose surface was scratched open to examine the iron layer deposited on it.

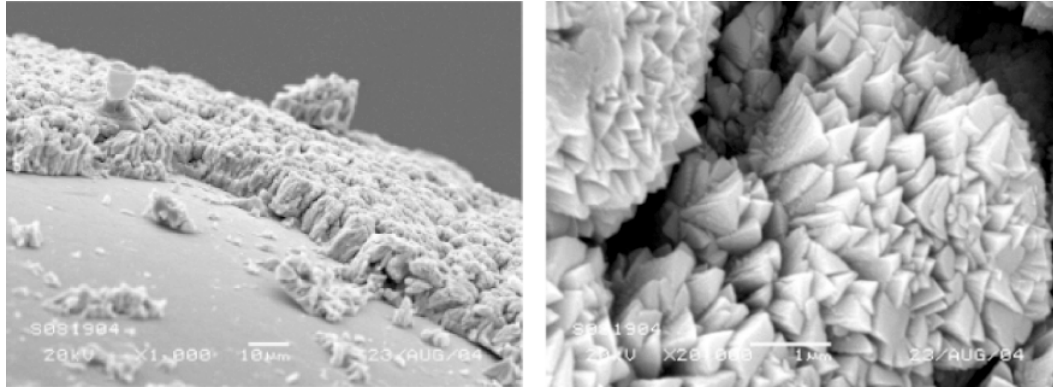


Fig. 5-1. Scanning electron microscopy (SEM) image of  $\sim 7 \mu\text{m}$  thick iron coating on  $1200 \mu\text{m}$  sapphire ball.

We also employed our sputter deposition system to bounce-coat  $1200 \mu\text{m}$  poly- $\alpha$ -methylstyrene (PAMS) shells with chromium. Figures 5-2 and 5-3 show a section of the wall of one of the chromium coated PAMS shells we fabricated.

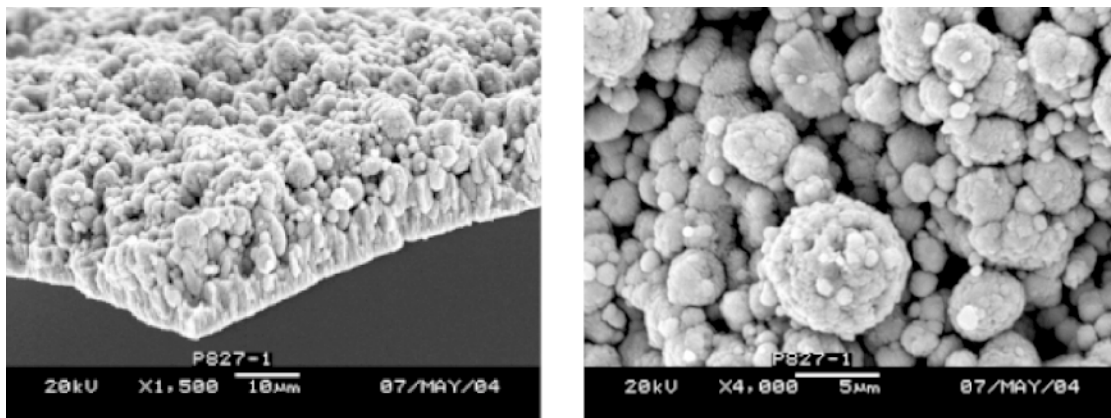


Fig. 5-2. SEM images of chromium layer deposited on PAMS shell.

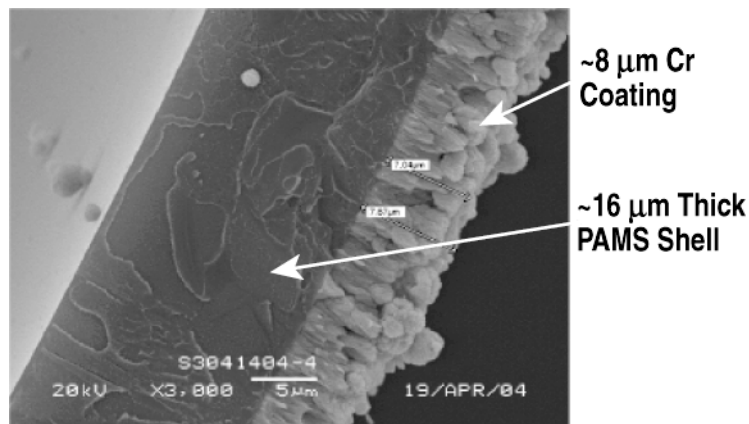


Fig. 5-3. SEM image of wall cross-section of chromium coated PAMS shell.

We tested the porosity of the chromium layer by pyrolyzing one of the shells under nitrogen at 300°C. Under these conditions, the PAMS layer decomposed and did in fact out-gas through the chromium layer, resulting in a free-standing chromium shell. Future work on both iron and chromium coatings will make use of an ion gun deposition system now being brought on line. This system should allow us to improve the surface finish of the deposited metals.

We enhanced our characterization capabilities for LANL by extending the measurement range of our atomic force microscope (AFM) sphere/wallmapper system down to 200  $\mu\text{m}$  diameter shells. To do this, we replaced the standard micromachined gold plated vacuum chuck with one made from a drawn glass capillary tube. Figure 5-4 shows a shell held on the new glass vacuum chuck in position to be characterized.

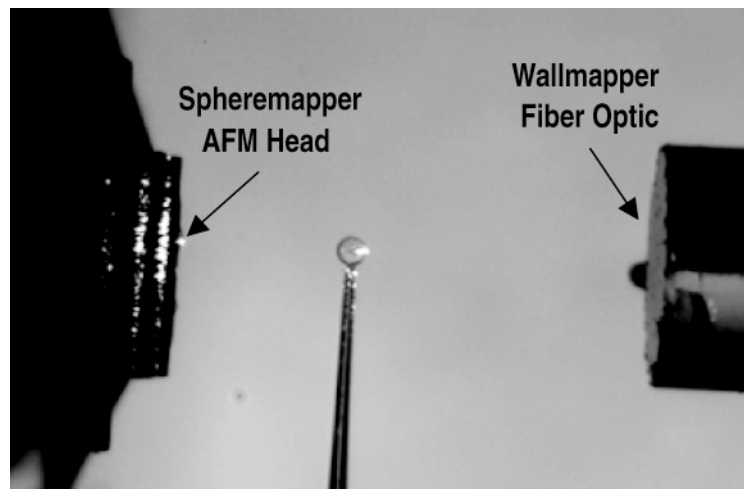


Fig. 5-4. We expanded the capabilities of our sphere/wallmapper system by fabricating a glass vacuum chuck small enough to hold 200  $\mu\text{m}$  shells.



## 6. 04LA03 FOAM SUPPORT (K. SHILLITO)

Task Leader: Kelly Youngblood

### Target Fabrication

During GFY04 LANL endeavored to establish technology to synthesize low-density aerogel materials for future Campaign 10 target needs. Expertise exists at Ocellus Technologies to synthesize aerogels of the densities and physical characteristics that are needed in future LANL Campaign 10 targets. Ocellus possesses expertise in the required equipment and process chemistry to synthesize low-density aerogel materials. LANL implemented this task with GA/Schafer, who sub-contracted with Ocellus Technologies to transfer aerogel synthesis expertise to LANL. During GFY03 an aerogel apparatus was designed and the equipment purchased. In GFY04 the apparatus was constructed, tested and delivered to LANL. The task also provided for further advice on the operation of the system as needed.

This task also fulfilled a need that LANL has to provide carbonized resorcinol formaldehyde (CRF) foam for experiments. Samples of CRF foam were delivered as needed for use in LANL experiments.

The main focus of this task was to install the silica aerogel reactor at LANL. Work was performed jointly with Dr. Mike Droege (Ocellus Technologies) providing the technological expertise. Many components purchased from various manufacturers were integrated into one easy-to-use system (Fig. 6-1). On site installation and training took place in August 2004 at LANL. Additional funds for the coming year have been allocated to continue Dr. Droege's technical support for the activation and process development of the aerogel reactor.



Fig. 6-1. Silica aerogel reactor.

LANL safety and performance requirements were met before the system was delivered. These requirements included the performance and safety checks of the organic vapor monitor; the HPLC pump; the vacuum subsystem; the valve actuator and selection; the computer with autoclave TowerView software; the actuator control tower; the individual temperature controllers and the ramp/soak programs. System setup required the resolution of many issues.

LANL also directed funds toward the production of CRF aerogel foams which were made in the Schafer foam laboratory. Over 150 individually characterized aerogel parts were produced for LANL's research team. There are continuing requests for this product and Schafer plans to install a new inductive heating furnace, which will offer more control of the carbonization process in the coming year.

## 7. 04LA04 MICROMACHINED TARGET COMPONENTS FOR LANL (J. KAAE)

In FY04, we produced 280 micromachined target components for LANL. The types of these components are listed in Table 7-1.

**Table 7-1**  
**Micromachined Target Components Produced for LANL**

<b>Component</b>	<b>Different Designs</b>	<b>Total</b>
Conventional hohlraums	2	36
Al Tubes	1	200
Au Tubes	1	20
Cu Disks	1	4
Al Disks	1	20

Of all of these components, the Al tubes were the most exacting to produce. They were made by first machining a copper cylindrical mandrel. These mandrels were then shipped to Alumiplate in Minnesota, where they were electroplated with aluminum. (Electroplating of aluminum is very difficult, requiring elevated temperatures and an inert environment. It is only carried out commercially at one place.) The electroplated mandrels were then shipped back to GA, where they had to be remounted in the diamond turning machine and machined to produce an aluminum band on the copper mandrel (Fig. 7-1.) The requirement was that there be less than  $2\ \mu\text{m}$  (preferably  $1\ \mu\text{m}$ ) difference in concentricity between the inner diameter of the aluminum band and the diameter of the copper mandrel. To achieve this, it required that the difference in alignment before and after aluminum plating be less than  $2\ \mu\text{m}$ . In spite of all of the handling of the parts, we achieved a success rate of about 75% in reducing the concentricity error to less than  $2\ \mu\text{m}$  and about 30% in reducing the concentricity error to less than  $1\ \mu\text{m}$ .



Fig. 7-1. Photomicrograph of aluminum band electroplated on copper mandrel.



## 8. 04NR01 NRL TARGET DELIVERIES (T. WALSH)

Task Leader: Tom Walsh

Target Fabrication

Scientists: Ed Hsieh, Katharine Nelson, Nicole Petta, Kelly Youngblood

Technicians: Sue Carter, Joe Florio, Josh Gregory, Derrick Mathews, Brian Motta

The Nike Laser at the NRL is designed only for experiments using planar targets, which are ideal for exploring material properties, hydrodynamic instabilities, and laser-target material interactions. The laser's beam is very uniform and well characterized so experimenters can explore the effects of depositing a large amount of energy in a material without perturbations from anomalies in the laser beam. For experiments to have meaningful results, the quality of the targets must at least equal the uniformity of the beam and exceed the limits of the diagnostic equipment. Over the years, as diagnostic equipment and prediction codes have improved, the requirements for target surface finish, uniformity, flatness, and purity have increased. Additionally, the complexity of target designs has increased by the addition of material layers, dopants, intentional surface and mass perturbations, and foams. NRL has also developed a cryogenic capability requiring targets that are designed to work in the wall of a cryogenic Dewar.

We discuss the activities associated with delivering and developing targets for NRL, especially:

- Smooth CH Films made of polystyrene and polyimide.
- Patterned CH Films with a wide range of sine wave periods and amplitudes. Some patterned targets were cast on molds, others had patterns machined directly into the foils.
- Coatings of various metals on polymer or polymer foam.
- NRL Foams of a variety of polymer types and densities.
- Nike EOS Targets which come in several varieties.
- Characterization of these targets.

**NRL Deliveries.** The past year has seen an increased emphasis on more complex targets (Fig. 8-1). The number of EOS targets increased as did the number of smooth targets. There was continued emphasis on foam, coated targets, and patterned targets.

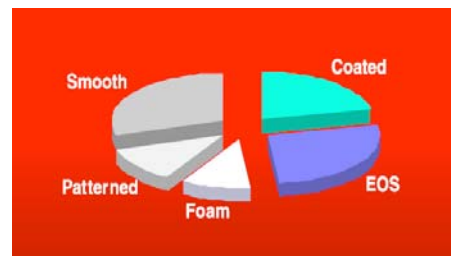


Fig. 8-1. FY04 target mix.

**Patterned CH Films.** A large portion of the films we delivered had a sine wave pattern on one surface. These films are made by machining the pattern directly into the foil or by casting the foil on a patterned substrate. Machining works well for patterns with peak-to-valley (PV) greater than one micron. For patterns with PV less than one micron, casting on an etched or machined mold usually gives better results. We have added a new technique to our characterization suite. By measuring the surface of the casting or mold with our Ambios stylus profilometer, we can analyze the pattern and tell if it is a pure sine wave or if it contains overtones. We started using this type of analysis because some of our gentec molds deviated significantly from a true sine. We calculated the effect of stylus radius on the sine wave analysis and found it to be negligible for the 25  $\mu\text{m}$  stylus we normally use. Table 8-1 is a list of molds currently available for casting at Schafer Laboratories.

**Table 8-1**  
**List of the Patterned Substrates Currently Available**  
**at Schafer for Casting**

Plate or Design	Surface Function	Period ( $\mu\text{m}$ )	Amplitude ( $\mu\text{m}$ )
Gnd Quartz #3	Ground with 3 $\mu\text{m}$ grit		
Gentec #01B	Sin(x)	12.0	0.23
Gentec #01C	Sin(x)	12.1	0.28
Gentec #01D	Sin(x)	12.1	0.31
Gentec #06	Sin(x)	20.0	0.25
Gentec #11	Sin(x)	20.0	1.00
Gentec #08b	Sin(x)	30.0	0.25
Gentec #08a	Sin(x)	30.0	0.26
Gentec #07	Sin(x)	30.0	0.10
Gentec #08	Sin(x)	30.0	0.25
Gentec #09	Sin(x)	30.0	0.50
NPL01	Sin(x)	30.8	0.94
Gentec #03	Sin(x)	60.0	0.10
Gentec #04	Sin(x)	60.0	0.25
Gentec #14	Sin(x)	60.0	0.47
Gentec #15	Sin(x)Sin(y)	20.0	0.23
Gentec #12	Sin(x)Sin(y)	30.0	0.10
Gentec #16	Sin(x)Sin(y)	30.0	0.26
Gentec #13	Sin(x)Sin(y)	60.0	0.10
Gentec #17	Sin(x)Sin(y)	60.0	0.23

**NRL Foams.** The primary ICF target design for NRL includes low-density foam. We now have resorcinol formaldehyde (RF) and divinylbenzene (DVB) foam production in place at Schafer Livermore Laboratories. Additionally we have the capability to make CRF, TPX,

polystyrene foam, and other foam systems in Livermore. Different foam systems range in densities from 3 to 850 mg/cc and pore sizes from nanometers to 15  $\mu\text{m}$ . During the past year we have continued to produce composite RF foam/polystyrene targets with a machined sine wave at the interface between the two materials. We have also produced doped foams using various doping techniques. Dopants have been added as physical dispersions by mixing small amounts of nanopowders uniformly throughout the foam. We have also doped foam systems using chemical modifications. Chemically doped monomers, polymers modified by chemical vapor deposition, or dissolved organometallics in the solvent system are all examples of doping by chemical modification. Foams with graded dopant concentrations have been produced by building the foam layer by layer with changing dopant concentrations in each layer. Work must still be done to learn how to properly characterize foam density uniformity, cell size uniformity, surface finish, and dopant concentration and profile. Table 8-2 is a summary of Schafer-produced foam types and their characteristics.

**Table 8-2**  
**Schafer Livermore Foam Systems**

Foam	Density Range (mg/cc)	Pore Size	Dopants	Chemical Composition	Production Issues
HIPE polystyrene	15–700	1–10 $\mu\text{m}$	Halogens Physical dispersions Embedded objects	CH	Molded or machined to shape Vacuum dried
Resorcinol-formaldehyde aerogel	20–850	nm	Chemical modification Physical dispersions	62 wt%C, 38 wt%O&H Carbonized 93 wt%C	Molded to shape Supercritical extraction Carbonized is machinable
Silica aerogel	10–700	nm	Chemical modification Physical dispersions	Si O	Molded or machined to shape Supercritical extraction
DVB	15–200	1–2 $\mu\text{m}$	Deuterated	CH	Supercritical extraction
TPX	3–250	1–15 $\mu\text{m}$	Physical dispersions	CH <sub>2</sub>	Molded or machined (higher densities) to shape

**Characterization.** Making targets to precise specifications is critical to the success of ICF experiments — just as critical is characterizing the targets precisely. We have expanded and modernized our characterization suite to include a Filmmetrics film mapper (Fig. 8-2), a Nikon NexIV automated measure scope (Fig. 8-3), a Nikon confocal microscope, and an Ambios stylus profiler (Fig. 8-4). These instruments will greatly improve our characterization accuracy and speed.



Fig. 8-2. Filmetric film mapper.



Fig. 8-3. NexIV automated measure scope.



Fig. 8-4. Ambios stylus surface profiler.

## 9. 04SL01 TARGET COMPONENTS AND CAPSULES (D. STEINMAN, J. KAAE)

### 9.1. Micromachined Components

In FY04, 208 micromachined target components were produced for SNL. The types of these components are listed in Table 9-1.

**Table 9-1**  
**Micromachined Target Components Produced for SNL**

Component	Different Designs	Total No.
Au hohlraums	3	24
Al stepped plates	2	18
GDP stepped plates	3	14
Polyimide stepped plates	1	6
Thin Al tubes	1	6
Small Al disks	1	39
Thick Al tubes	1	15
Cu lined Au hohlraums	1	6
Cu cryo fixtures	3	15
Thin Al tubes	3	3
Au cones	4	21
Fiducial crosshairs	1	15
Au washers	1	10
Epoxy rings	1	6
Capsule mandrels	1	6

As can be seen from Table 9-1, these target components were made up of a few of many different types. To demonstrate this diversity, a number of the components are shown in Figs. 9-1 through 9-5.



Fig. 9-1. Gold hohlraum on the copper mandrel, which will be dissolved out subsequently. The shape is unusual with two different diameters and an off-axis hole in the face of the large diameter section.

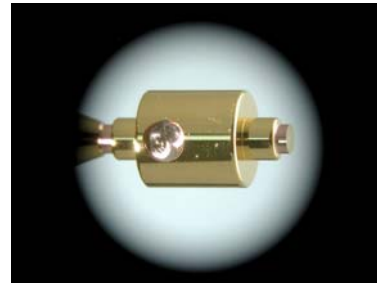


Fig. 9-2. Gold hohlraum on the copper mandrels, which will be dissolved out subsequently. The shape is unusual because of the sections with different diameters and the large hole in the side of the large diameter section.



Fig. 9-3. A complex copper fixture to be used in cryogenic double-shell tests.



Fig. 9-4. A very thin aluminum foil.

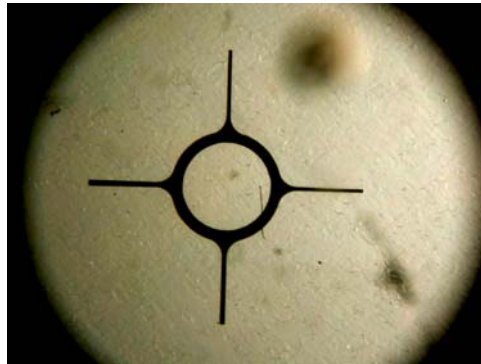


Fig. 9-5. A gold fiducial ring with thin spacing extensions.

## 9.2. SNL Capsule Production

SNL capsule production in FY04 saw the introduction of two new target types: Gold shim targets and CH shells having a glass permeation barrier. Both of these target types required extensive development and challenged us to meet delivery deadlines. We also made significant improvements in the characterization of “standard” SNL 2 mm CH capsules that use polyvinyl alcohol (PVA) and aluminum layers as gas fill permeation barriers.

The Table 9-2 lists the capsule deliveries for SNL in FY04.

In accordance with our ISO 9001 commitment to “continuous improvement” we developed a better method to characterize the wall thickness and uniformity of 2 mm SNL capsules. We did this by using x-radiography in conjunction with our automated NEXIV microscope.

In FY03, we used interferometric microscopy to measure SNL capsule walls at a dozen points around the equator. This manual procedure was slow and meticulous and the data it provided was of limited value. Our new procedure consists of taking an x-radiograph of the

capsule (Fig. 9-6) and programming our automated microscope to measure the shell wall thickness at 3600 points around the equator from the x-radiographic image.

In previous years for LANL and LLNL targets, we determined the wall thickness of 0.5 mm CH shells from a single digitized x-ray image of the entire shell. Because SNL capsules are an order of magnitude larger in size, we are instead using our automated microscope at a high magnification that only images a small portion of the shell wall for each measurement (Fig. 9-7). In this manner, the resolution of the wall thickness measurement is maximized.

**Table 9-2**  
**SNL FY04 Capsule Deliveries**

Target Type	Orders	Capsules
2 mm x $\sim 60 \mu\text{m}$ multi-layer shells (GDP-PVA-GDP-Al-GDP)	12	95
5 mm Ge-GDP shells w/ gold shim	4	25
3 mm x 50 GDP w/ $2 \mu\text{m}$ glass layer	1	8
1600 x 40 Hoppe glass (development task)	1	NA
2 and 3 mm CH Hemi-shells	<u>3</u>	<u>22</u>
Total	21	150

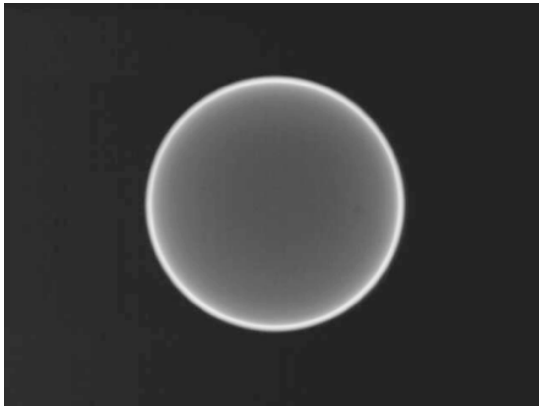


Fig. 9-6. X-radiograph of 2 mm SNL capsule. The capsule is oriented such that any wall thickness variation resulting from the PVA coating process will be revealed.

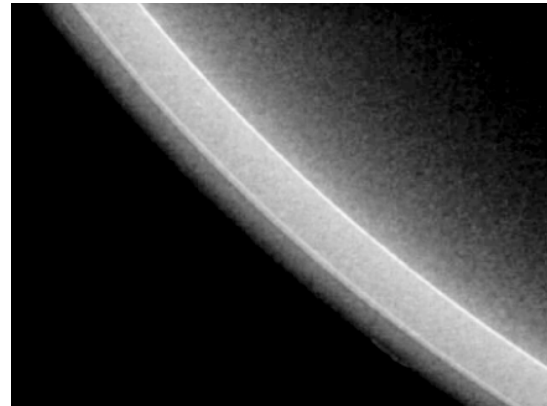


Fig. 9-7. X-ray image of a  $\sim 50 \mu\text{m}$  walled SNL capsule. Rather than analyzing the image of the entire shell at low magnification, the NEXIV microscope measures wall thickness at high magnification to enhance resolution. (Note the PVA layer in the middle of the shell wall.)

We programmed our automated microscope to take 3600 wall thickness measurements around the shell circumference. Every 10 successive data points were averaged to reduce the noise. Figure 9-8 shows the average wall thickness and the thickness variation of a typical

2 mm SNL shell. The wall thickness variation is indicative of the non-uniform “dip and spin” PVA coating process.

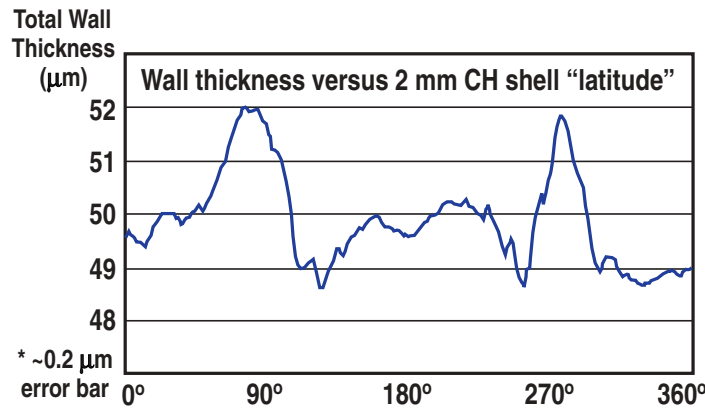


Fig. 9-8. Capsule wall thickness plot generated from 3600 measurements taken by our automated microscope from the x-radiograph of a 2 mm SNL capsule.

The wall thickness data we generated confirmed that the use of a PVA permeation barrier on SNL capsules resulted in undesirable wall thickness variations. Partly for that reason, we developed a  $\sim 2 \mu\text{m}$  thick glass permeation barrier to replace the PVA. The first glass-coated CH capsules were delivered to SNL late in FY04. They had a glass layer thickness variation of less than  $0.2 \mu\text{m}$  as determined by our wallmapper system.

Glass is also superior to PVA as a gas barrier for retaining hydrogen isotope fills in ICF capsules. The deuterium fill H-Ls of the glass-coated capsules we delivered to SNL was over a month in duration, far longer than that of composite PVA/aluminum permeation barriers. Eventually, tritium-filled capsules will be requested for SNL experiments. Unlike PVA, which is degraded by radiation from a DT fill, glass has been shown to retain its good gas retention characteristics. A detailed discussion of our glass permeation barrier development work can be found in Section 17.1 along with a discussion of how we have employed our mass spec system to measure capsule H-Ls.

## 10. 04SL02 TARGET FABRICATION (D. SHROEN)

04SL02 is an onsite task supporting target fabrication. It is imperative for this work to occur at SNL as it allows for direct interaction with the experimenters, close collaboration with the other groups of supporting technologies, and eliminates the need for transport of fragile target assemblies. The staff is composed of eight individuals: Eric Breden and Suzi Grine-Jones (target assemblers), Justin Stolp and Randy Holt (documentation and quality control), Chris Russell (production planner and coordinator), Wojtek Krych, Jon Streit, and Diana Schroen (chemists). There is also support at the Schafer Livermore office from machining staff, Joe Florio and chemist support, Kelly Youngblood.

The workload at Sandia continued to increase this year as the shot rate increased slightly (from 196 in FY03 to 204 in FY04) and the complexity of the targets greatly increased. One measure of the increased complexity is to examine the number of target component parts that were required for assembly. The number of parts processed per month is shown in Fig. 10-1. While there is some month-to-month variation, the trend is distinctly for more parts per month.

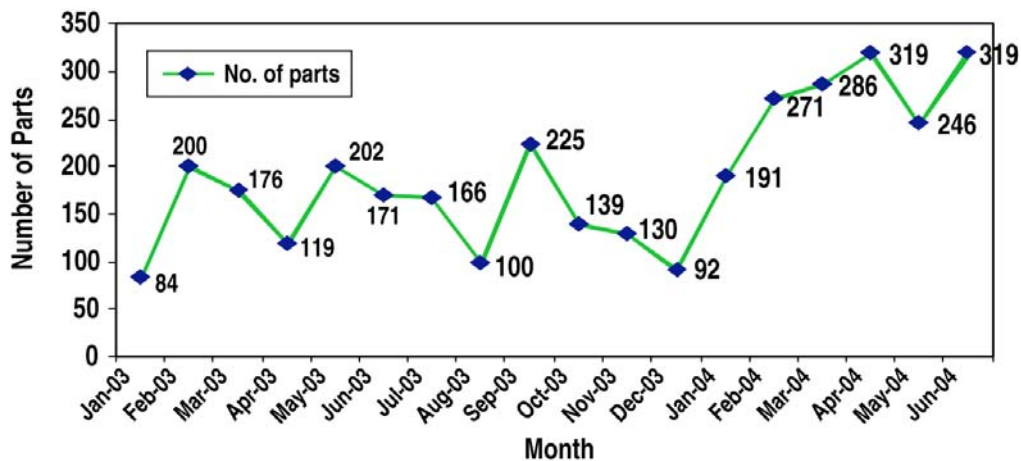


Fig. 10-1. Graph of parts processed per month by on-site personnel at SNL. Months with lower numbers, due to two work stoppages: one for beryllium issues the other for improving target component ID and traceability process.

There were four technical target issues we addressed this year. The first issue concerned the assembly of the double pinch hohlraum. The size of the capsule in this target was increased to as large as 5 mm. At this size, our standard procedure of mounting the capsule between two Formvar films was no longer satisfactory. The Formvar films had been mounted to one frame so the films had much curvature and major wrinkling. The wrinkling imprinted upon the capsule during the compression of the capsule was unexpected as each film was  $\sim 0.3 \mu\text{m}$  thick. Our solution was to make two frames and use a spacer to hold the frames apart — a distance just slightly smaller than the diameter of the capsule. This held the capsule in place without major deformation of the Formvar (Fig. 10-2).

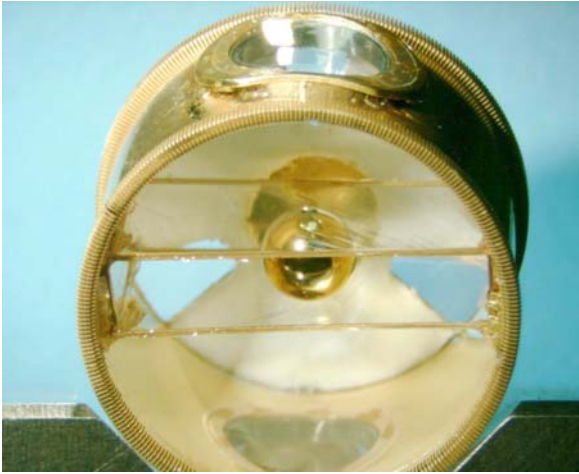


Fig. 10-2. An end on view of the capsule in the secondary hohlraum of a double pinch target. The two frames and the offset minimize the deformation of the Formvar.

a cut was made just below the gold band and the copper mandrel was dissolved away. This was more successful as several free-standing hemis were produced and assembly was attempted. Unfortunately, the gold ring became detached from the hemi thus allowing it to deform as before. Work on this target will continue into the next year.

The third challenge was to produce TPX foams with new dopants, specifically molybdenum, titanium and a dual dopant of titanium and chloride. We had previously produced foams with nano-particles (Au) and organo-metallics (Si). The organo-metallic route is the simpler of the two processes, thus we chose that route for the new dopant request. With this technique, the dopant is distributed in molecules so there is no agglomeration. The only requirement is that the molecules must be soluble in cyclohexane, the solvent we use for creating TPX foams. The organo-metallics used were cyclopentadienylmolybdenum tricarbonyl dimmer, titanium (IV) isopropoxide and chlorotitanium triisopropoxide.

The fourth challenge was also a foam technology. We were requested to create a shaped foam with an embedded capsule for a dynamic hohlraum experiment. The foam was to have a wider diameter around the capsule, see Fig. 10-4 below. The complications added by the shape include, (1) the capsule centering in the length must be much more precise, (2) the density uniformity is more difficult as the mold is two pieces, and (3) removing the foam from the shaped mold is more difficult and more foams are lost at this stage.

The second technical challenge was to fabricate a double hemispherical fast ignitor target. This was expected to be difficult and as such was a developmental task. The goal was to build a target with an outer hemisphere of 2.7 mm o.d. and a wall of  $60\ \mu\text{m}$  and an inner hemisphere of 2.5 mm o.d. and a wall of 3 to  $4\ \mu\text{m}$  as shown in Fig. 10-3. We began by taking the simplest route — cutting a thin walled capsule at the midpoint. Unfortunately this deformed the capsule and resulted in a hemi too fragile to mount, especially as there were often small cracks originating from the cut edge. The next fabrication route we tried was to make a copper mandrel, incorporate a gold ring at the base and coat with GDP. After coating,

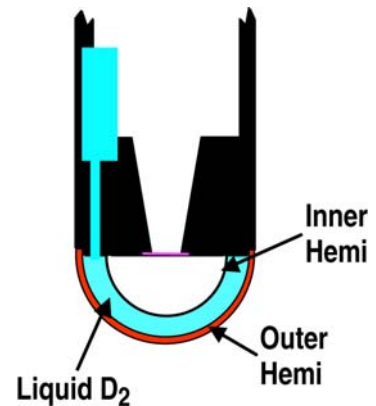


Fig. 10-3. Schematic of the fast ignitor target design.

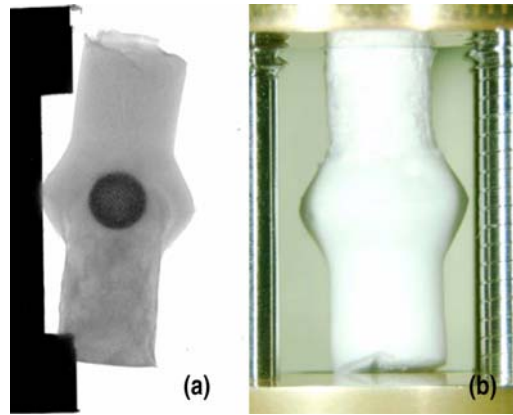


Fig. 10-4. (a) A radiographic image of a shaped foam, (b) is the same foam in the early steps of target assembly. The shape of the expanded diameter is a cosine function specified by the experimenters.

For further information contact Diana Schroen at [dgschro@sandia.gov](mailto:dgschro@sandia.gov).



## 11. 04UR01 TARGET PRODUCTION AND DELIVERY (A. NIKROO)

### 11.1. Center for Coatings, Polymer and Foam Shell Development

#### 11.1.1. Introduction

We report on the major activities of the Center for Coatings, Polymer and Foam Shell Development in FY04. Our major task in FY04, as in the previous years, was the support of on time delivery of targets requested by all the various DOE ICF labs. Our group was responsible for two essential operations in achieving this task: PAMS shell production and GDP coatings, necessary for fabrication of the variety of requested capsule and flat targets. PAMS batches were manufactured to stock our inventory of mandrels and as needed for individual orders. Doped and undoped GDP coatings were deposited on a variety of substrates, mainly shells, in the course of fabrication of the majority of the targets delivered.

In addition, we had the administrative task of coordinating the target delivery requests for University of Rochester's Laboratory for Laser Energetics (UR/LLE). We report on the LLE deliveries in Section 11.1.1 and outline the various types of targets delivered to LLE. The various FY04 UR/LLE's deliveries are categorized by type and difficulty in Section 11. Through the data and knowledge bases accumulated over the past several years, fabrication of many of the previously challenging and time consuming targets for UR/LLE has become routine. In Section 12, we present a brief summary of the developmental effort supported by a contract from UR/LLE to investigate fabricating advanced foam targets and CH shells with monolithic fill tubes. A number of indirect drive NIF target fabrication issues were examined as well by our group in FY04. Production of NIF quality full thickness GDP (CH) shells was examined in FY04. The results of this developmental effort are summarized in Section 17. We also began work towards fabricating beryllium shells suitable for shots at SNL's Z facility in FY04. This development is discussed in Section 20. Finally, in Section 17, we report on the capabilities improvement effort, which is geared towards developing new fabrication or characterization techniques that have general benefit and can improve the quality of the targets or the associated characterization data.

#### 11.1.2. UR/LLE Deliveries

In FY04, our group continued coordinating delivery of targets to UR/LLE. Delivery requests were received from UR/LLE points of contact and processed through the various steps of fabrication to ensure on time delivery. Final target data were sent to LLE electronically via e-mail as well as posted onto a password protected web site accessible by LLE personnel. A total of 1129 targets in 62 separate orders were delivered to UR/LLE for shots on the OMEGA laser as detailed in Table 11-1. For comparison, Table 11-1 shows FY03 deliveries. Virtually every request was delivered on time as shown in Fig. 11-1, with most delivered many days in advance of the requested date to allow more time on onsite assembly and processing at LLE. The different types of capsules delivered as part of the orders mentioned above are categorized in Fig. 11-2. Figure 11-2(a) plots the deliveries

according to the number of orders (or batches) delivered, while Fig. 11-2(b) shows the number of shells provided for each type. In addition, in the figures, the deliveries are broken into the different major classes of shells requested. The different classes are plotted in the order of increasing fabrication difficulty.

**Table 11-1**  
**LLE Target Deliveries in FY04**

Type	Orders	Requested	Delivered
Capsules	55	1013	1059
Planar foam	5	71	79
$\mu$ -machined	2	45	52
FY04 Totals	62	1129	1190
FY03 Total	61	1154	

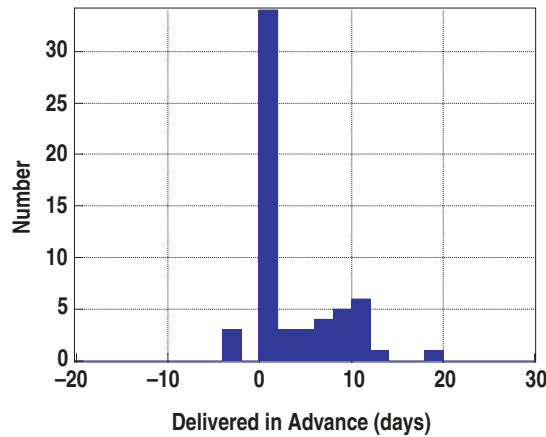


Fig. 11-1. We continued our responsive, on time target deliveries to LLE. Ninety-five percent of orders were delivered on time or early.

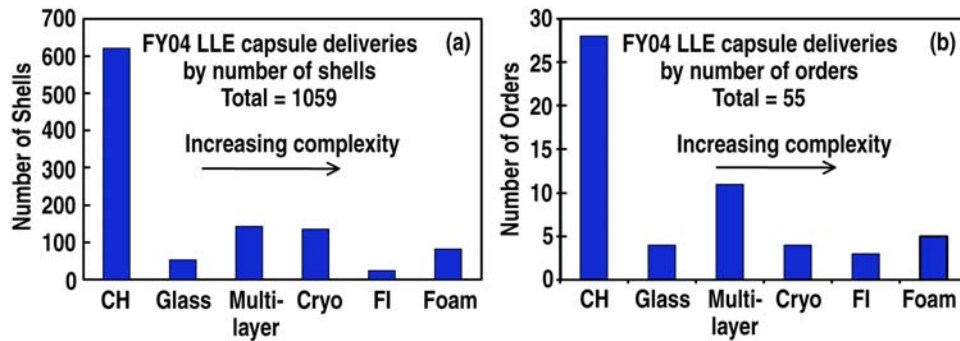


Fig. 11-2. The various types of capsules delivered broken up into characteristic groups by number of orders (batches) made in (a) and by the number of capsules delivered in (b). Plain CH shells comprised the majority of the fabricated capsules, but the fewer more complex capsules such as foam and fast ignition (FI) required as much effort in fabrication due to their higher complexity.

Routine types, mainly plain CH (and CD) shells, ~ 15-35  $\mu\text{m}$  in wall thickness, are those that can be made in a relatively short period of time and with a minimum of effort. Transitional types mainly consist of multi-layer and thin wall cryogenic shells. While the major development on these types has been completed, they still involve multiple manufacturing and testing steps and require more effort. As part of our delivery activities, we also performed extensive mechanical and permeation testing of thin wall shells used for cryogenic shots for quality control. This information is necessary to ensure consistent shell quality for the successful high pressure filling and cryogenic cooling at UR/LLE. The developmental types involved foam and FI shells. Foam shells became a regular request item in FY04. The developmental efforts in FY02-FY04 on foam shell fabrication enabled production type delivery of these targets in FY04. In addition to foam shells, we also delivered a variety of flat foam targets overcoated with GDP and foam-filled cylinders. The highlights of foam shell development are given in Section 12. We also continued to deliver gas retentive FI targets for the first time shot at OMEGA as part of LLE's effort. These targets are also developmental involving a shell mounted on a gold cone. The new developments in this area dealt with making the targets gas retentive and the related characterization of the assembled targets. The reader is referred to Ref. 11-1 for the details of this developmental activity.

Deliveries of developmental types are more challenging and usually require more lead-time and substantially more manpower. Our goal has been that in time the transitional and developmental targets will become routine. Figure 11-2 point out that the effort involved in providing all the needed targets depends not only on the number of shells or orders delivered but the difficulty involved in fabrication as well. For example, although there were fewer foam or FI shell requests, the fabrication effort for them was equivalent to that of providing the larger number of plain CH or CD shells.

In addition to the deliveries above, we also provided a variety of targets as "samples". These were either shells or flat samples provided to UR/LLE for uses mainly other than laser shots.

### References for Section 11

[11-1] D.W. Hill et al., Fusion Sci. Technol. **45**, 113 (2004).



## 12. 04UR02 CRYOGENIC CAPSULE DEVELOPMENT (A. NIKROO)

### 12.1. Foam Shell Fabrication

In FY02, we had embarked on a developmental effort to fabricate foam shells for future use at UR/LLE. Two types of foam shells are required. The first type, referred to as low density, is required to have a density of  $\sim 30$ -140 mg/cc and wall thickness of  $\sim 30$ -100  $\mu\text{m}$ . These shells would be used as the cryogenic “wetted-foam” targets which promise high yield. The second type, referred to as high density, has a density of  $\sim 180$ -250 mg/cc and wall thickness of 80-100  $\mu\text{m}$ . These are designed for room temperature shots to simulate the implosion behavior of cryogenic DT, which has a similar density, without doing cryogenic shots. A thin,  $\sim 1$ -5  $\mu\text{m}$ , CH gas permeation barrier is required for both types. An important specification is the shell wall thickness uniformity, which is specified to be less than 5  $\mu\text{m}$ . In FY04, this task was expanded to include fabrication of direct drive fill tube surrogate shells as well as investigating fabrication of cryogenic type shells with a monolithic fill tube. We present a summary of the progress achieved in FY04.

In the previous years, we had shown that we were able to fabricate low-density foam shells using resorcinol formaldehyde (RF) foam chemistry chosen as the chemistry of choice because it leads to transparent foam shells, which allows optical characterization of shells. In addition, we had shown that GDP coatings could be used as the permeation barrier. Such coatings led to gas retentive shells, with an acceptable yield of  $\sim 60$ -70%. We had also demonstrated fabrication of high-density shells; however, the wall uniformity had been poor, reducing the yield of target quality shells and batches of shells [12-1].

Our effort in FY04 concentrated on improving the wall uniformity of the high-density shells. Variations in the density matching of the different phases involved in the microencapsulation technique used for this work were investigated. In general, we found that a slight density mismatch was needed to obtain the best wall shell non-uniformity. This is shown in Fig. 12-1. However, wall uniformity of high-density shells was in general poorer than that of low-density shells. The percentage of shells with wall thickness non-uniformity of  $<10$   $\mu\text{m}$  was on average only  $\sim 5\%$  for the high density shells, compared to 25% for low-density shells. While this yield was low, it was sufficient to enable delivery of high density foam shells, as mentioned in Section 11.1.1, for shots on OMEGA.

In addition to developing high-density shells, we also developed and produced other types of foam targets. Foam-filled cylinders were requested for astrophysical experiments. The cylindrical sleeves, with  $\sim 10$   $\mu\text{m}$  parylene walls, were provided by LLE target fabrication group. A proper fixture was designed and built for holding the fragile sleeves to receive the foam solution, guaranteeing a flat surface at least at one end of the cylinder. Cylinders were filled with 100 mg/cc DVB and then dried in the critical point drier. The yield of the process is  $\sim 50\%$  currently and we hope to improve that in the future. A picture of such a foam-filled cylinder is shown in Fig. 12-2.

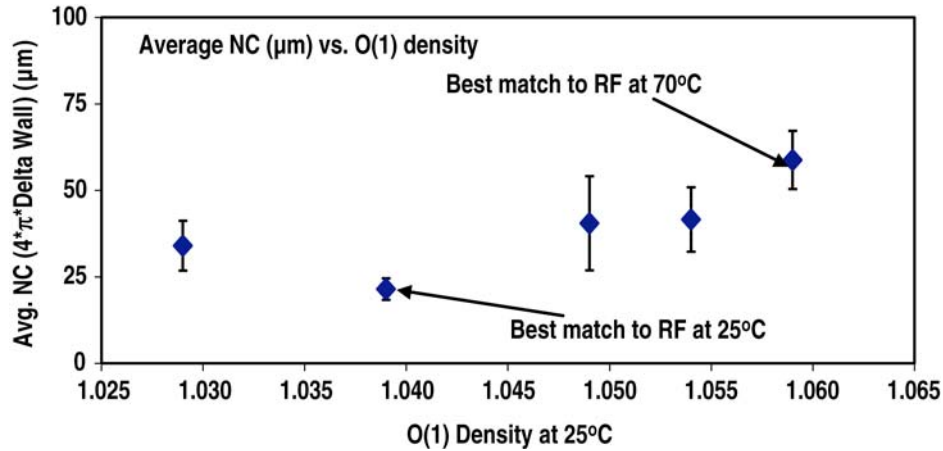


Fig. 12-1. Plot of NC versus delta density.

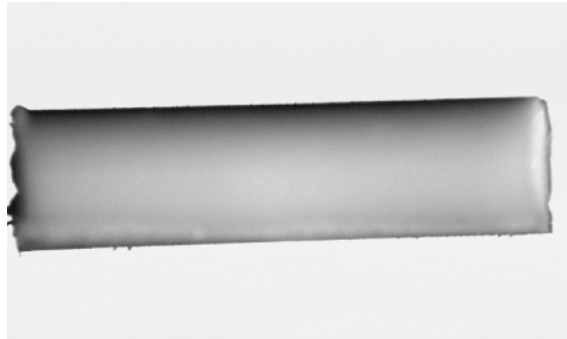


Fig. 12-2. Foam-filled cylinders became an often requested target in FY04. These cylinders, which consisted of 100 mg/cc divinylbenzene (DVB) foam-filled parylene sleeves, were initially developed under the foam development contract and then handed over to production.

Flat targets to simulate and study the growth of surface perturbations during compression of foam shells with a full density overcoat also were needed in FY04. A schematic of such a target is shown in Fig. 12-3. The requested wavelength was  $120 \mu\text{m}$  with an amplitude of  $\sim 1 \mu\text{m}$  for these initial targets. One method for fabrication of these targets involves fabrication of the two layers separately and then gluing them together. This allows machining of the CH layer prior to addition of the fragile, collapsible foam layer. Even so, it is difficult to machine  $\sim 3\text{-}4 \mu\text{m}$  thick CH layers as they are too thin to resist the forces of diamond turned machining. However, using molding technique we were able to make thin rippled CH layers with the desired wavelength and amplitude. Nevertheless, upon close examination of the interface between the foam and the full density layer by interferometry, even the best targets made using this gluing technique had slight gaps of a few microns between the layers. Other techniques such as directly molding the foam onto the thin rippled Ch films also failed due to excessive wrinkling of the thin films. Therefore, we decided to GDP overcoat the foam flats to avoid any gap between the layers. Then laser machining was used to directly machine the sinewave into full density GDP overcoat. To accomplish this, GDP overcoated

foam flats were mounted to plastic washers for support and taken to Exitech, Inc. in San Jose, California, for laser machining, using Exitech's mask dragging technique. Figure 12-4 shows a picture of a completed target. As can be seen, the plastic washer contained an  $\sim 1$  mm hole for accommodating the OMEGA laser shot. Figure 12-5, shows an interferometric image of the surface showing the sinewave-like ripples. The wavelength measured using the interferometer was  $\sim 120 \pm 10 \mu\text{m}$  as requested and the amplitude was within 20% of the desired  $1 \mu\text{m}$  value. The profile resembled a pure sinewave with a sharp peak at  $120 \mu\text{m}$  in the Fourier power spectrum and the second harmonics being over an order of magnitude lower in power. The yield of this technique is still low,  $\sim 20\text{-}30\%$ , due to several factors. Beyond the  $\sim 50\text{-}70\%$  yield in the foam flat fabrication process, a major one is the handling needed in getting the targets to Exitech, which we hope to avoid by acquiring such a unit at GA. The other is the curvature of the overcoated foam pieces due to internal stresses in the GDP, which causes problems in diagnosing the results at OMEGA and in laser machining the ripples at Exitech. This second problem has been alleviated by coating the pieces in coaters that deposit GDP with the lowest internal stress. The curving of the foam pieces is a good indicator of this internal stress. These targets are very labor intensive because of the various steps involved in their fabrication.

We also examined fabrication of low-density RF shells with larger pores. This appears to be necessary given the cryogenic  $\text{D}_2$  ice layering results at LLE, which indicate that the standard RF shell becomes foggy when  $\text{D}_2$  begins to freeze inside the

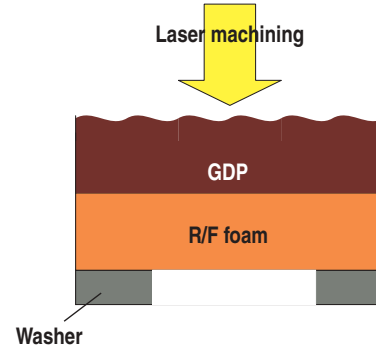


Fig. 12-3. Gapless foam-full density multi-layers flats were developed in FY04. The full density layer needs to have a sinewave pattern ( $\sim 120 \mu\text{m}$  wavelength,  $1 \mu\text{m}$  amplitude) on its free side. GDP coating of the foam flat eliminated any possibility of a gap between the layers and laser machining was used to generate the ripples. The GDP layer, exaggerated in the figure, was only  $3\text{-}4 \mu\text{m}$  in thickness and the foam layer was  $\sim 100 \pm 20 \mu\text{m}$  in thickness and  $200 \text{ mg/cc}$  in density. The foam-GDP combination was glued to a washer with a large enough hole to accommodate the OMEGA laser beam and diagnostics view.

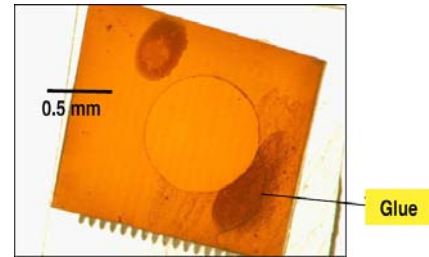


Fig. 12-4. Photo of a completed target shot at OMEGA. The hole in the washer is clearly visible along with the glue spots (dark spots) used to fix the composite to the washer. The sinewave pattern is barely visible in the central hole region.

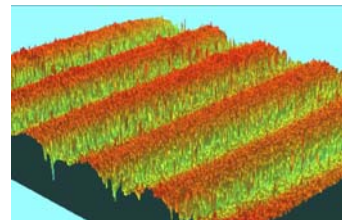


Fig. 12-5. White light interferometer 3D profile of the target in Fig. 12-4. The profile resembled a sinewave closely, with  $\sim 120 (\pm 10) \mu\text{m}$  wavelength and  $\sim 1 (\pm 0.2) \mu\text{m}$  amplitude.

foam. It is believed that this fogginess is the result of inadequate wetting of the standard RF foam due to its very small pore size ( $\sim <100\text{\AA}$ ). To fabricate larger RF foam we used the same chemistry as standard RF, but increased the reaction rate of the components, hastening the gelation of the foam. This would lead to larger pores as reactant would not have time to inter-diffuse as much as the case of standard RF. By doing so, we indeed did make RF foam with larger pore size as shown in Fig. 12-6. It is very difficult to obtain a quantitative measure of the difference in the pore size of the two different types, but a qualitative difference can be immediately seen. In addition, while the standard RF was clear and very much light transmitting, the RF foam made using the modified procedure was more hazy and less light transmitting, due to enhanced visible light scattering by the larger pores. Shells were then made using the larger pore RF. Figure 12-7 shows the difference between shells of the two different types. The black line in the figure is under the shells, and the lower light transmission of the shell on the right is an indication of the larger pore size and more scattering. However, despite higher level of visible light scattering, the large pore shell is still highly transparent for visible light characterization. The major problem with this process currently is the much poorer wall uniformity of the shells (see Fig. 12-7 for example). The faster gelation used for higher pore RF freezes the inner core of the microencapsulated RF foam before it has a chance to center itself, making a uniform wall foam shell. This may be a fundamental issue with this technique, but our work in future will be focused on addressing this issue. The other issue with these shells was that we found that the GDP overcoating used to seal the foam shell for gas fills, not surprisingly, needed to be much thicker,  $\sim 10\ \mu\text{m}$ , compared to  $\sim 4\ \mu\text{m}$  for standard smaller pore RF. Nonetheless, gas retentive, GDP overcoated large pore RF shells were fabricated and sent to LLE for cryogenic studies and

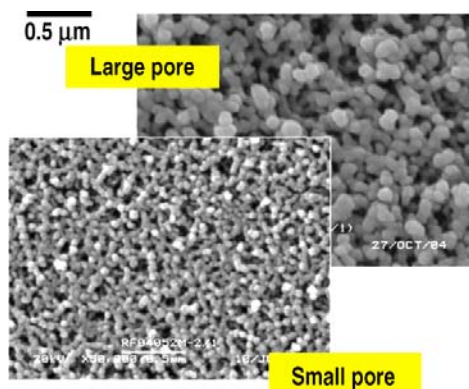


Fig. 12-6. Electron microscope images of standard pore RF foam (foreground) and modified, larger pore RF (background) both at  $\sim 100\ \text{mg/cc}$  density. The scale is the same for the two images as indicated. The larger cells are quite apparent in the image as well as the increased thickness of the foam strands for the larger pore foam.

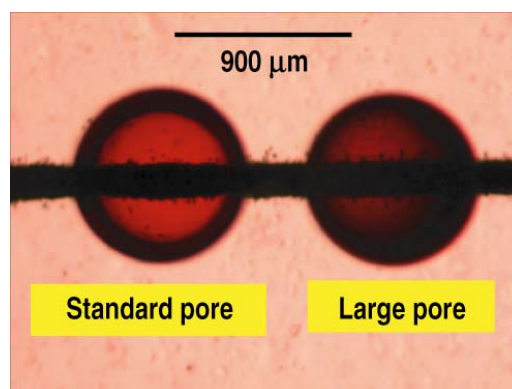


Fig. 12-7. Photo of RF shells made using standard pore RF (left) and large pore RF (right). The photo was taken with light transmitting through the shells. The black line was drawn behind the shells to indicate that although there is more light scattering due to the larger pore size of the shell on the right, it is still transparent enough for visible light characterization (the line is still clearly visible through the shell). Note that the large pore shell (right) has a noticeable wall thickness non-uniformity.

early indication is that the larger pores helped in more fully filling of the foam with  $D_2$ , yielding a clearer view of the ice formation.

Another possible large pore foam is DVB. DVB has pore size of  $\sim 0.5$  to several microns. With the need for larger pore foam, we also examined fabrication and overcoating of DVB shells for LLE. We had made DVB shells in the past and we used similar techniques to make shells in the OMEGA size ( $\sim 900 \mu\text{m}$  diameter) in large quantities (Fig. 12-8) needed for further processing. One major issue with DVB shell fabrication had been the excessive cracking of these shells upon fabrication. Almost all shells within a batch may be cracked, making the process useless for production of shells to be used in experiments. In FY04, we developed a new process for fabricating DVB shells, which resulted in a much higher yield. This modified process allows extended cross-linking of the DVB matrix, which in turn prevents cracking of shells and results in a higher yield. The other major issue with DVB was obtaining a proper gas tight coating. GDP could not be used directly as in RF. While it did cover the sub  $0.1 \mu\text{m}$  pores of the RF foam, it would not cover the larger pores of the DVB foam. Interfacial coating such as polyvinylphenol (PVP) was therefore attempted. We were able to deposit PVP on DVB, however, the yield of gas retentive coatings was very low,  $\sim 10\%$ . Gas retentiveness of these shells was measured using the mass spectrometer system described in Section 20, illustrating the benefit and wider applicability of the capability enhancement work described in that section. Therefore, we decided to add a GDP coating on top of the PVP coating in hope of better closure of the pores (see Fig. 12-9). This indeed did increase the yield of gas retentive shells dramatically to  $\sim 80\%$ . Such shells were made and sent to LLE for cryogenic testing, which will take place soon.

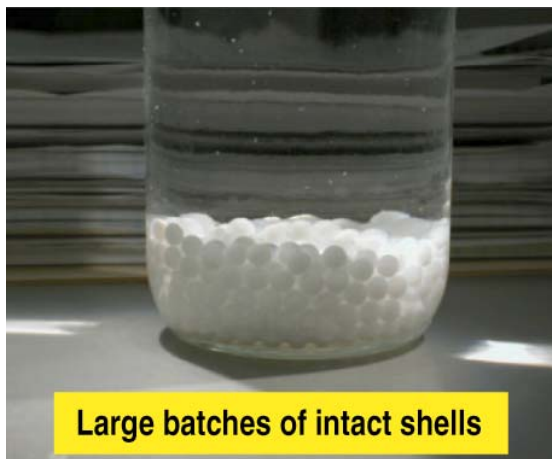


Fig. 12-8. Large batch of DVB shells made using a modified microencapsulation procedure. Such large batches were virtually crack free, a major limitation in DVB shell fabrication previously. This provides a sufficient number of shells for further processing, such as overcoatings and deliveries for experiments at LLE.

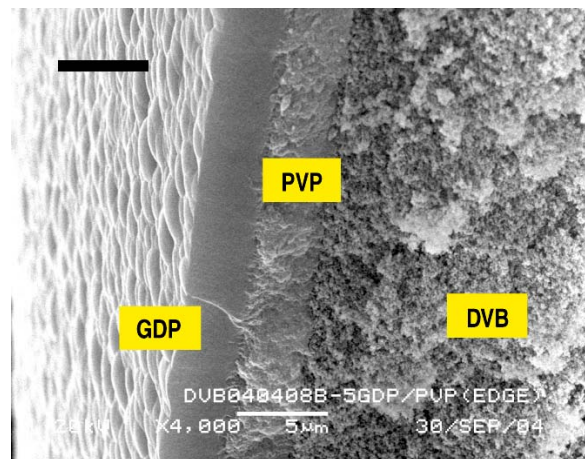


Fig. 12-9. Cross-sectional electron microscope image of a PVP + GDP coated DVB shell. The black scale bar is  $5 \mu\text{m}$ . Each coating layer is  $\sim 4 \mu\text{m}$  in thickness. The PVP-GDP combination had to be used to increase the yield of gas retentive shell from  $\sim 10\%$  with only PVP coating to  $\sim 80\%$  using the combination.

Finally, we discuss our initial work towards making a monolithic thin walled CH fill tube target. This target may become necessary due to fast track ignition, which involves a cryogenic system that can only accommodate fill tube targets. To make a monolithic fill tube target, we would use the “tail pulling” technique of Jon Burmann, Ref. 12-2, as illustrated in Fig. 12-10. The tail on the PAMS shell is added by briefly touching the PAMS shell to a molten pool of PAMS and pulling the shell to draw a fiber-like tail. In FY04, we concentrated on making the contact spot and the tail diameter near the contact point as small as possible,  $\sim \leq 15 \mu\text{m}$ , as this is the key criterion for NIF targets. We also produced fill tube surrogate targets as discussed below. We were able to make a number of shells with the required contact spot of  $\sim 15 \mu\text{m}$  with short stubby tails of  $\sim 50\text{-}80 \mu\text{m}$  long. These shells were then overcoated with GDP as required, but the tail was not cut off prior to pyrolysis to yield a close end tube. This process produced so-called fill tube surrogate targets, which were sent to LLE for cryogenic  $\text{D}_2$  experiments (Fig. 12-11). The fill tube surrogate targets were therefore all checked for gas retentiveness ensuring that the fill tube end was indeed closed by the GDP coating. Initial shots at LLE examining the effects of fill tubes were performed using these targets.

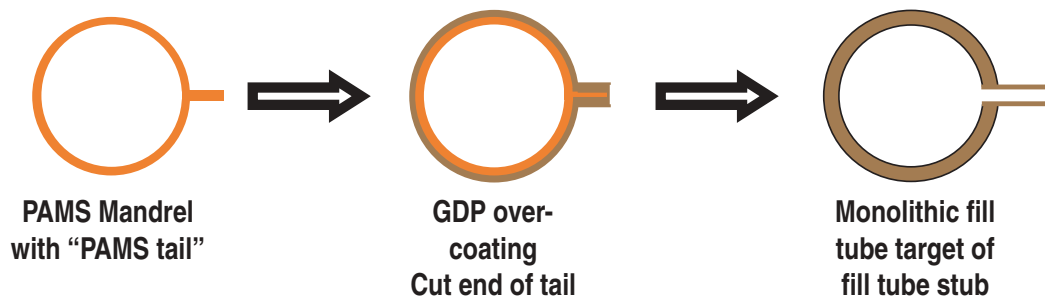


Fig. 12-10. The PAMS/GDP technique to make monolithic fill tubes. The “PAMS tail” is attached to the PAMS mandrel using the techniques described in Ref. 12-1. If the tail is not cut before pyrolysis, then a closed end tube is obtained.

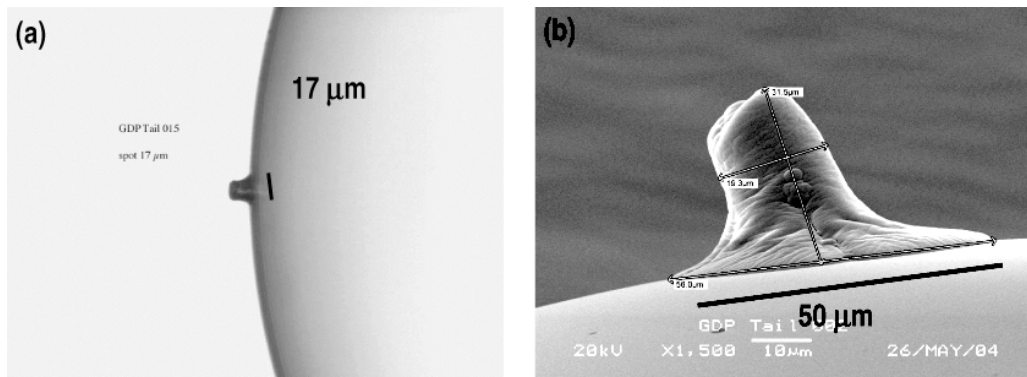


Fig. 12-11. Closed end fill tube surrogate made using the technique shown in Fig. 12-10. These targets were shipped to LLE and were fielded cryogenically and shot to examine effects of fill tubes on implosion. All targets made this way were examined for gas retentiveness before delivery to LLE. (a) Optical picture of a closed end tube with  $\sim 17 \mu\text{m}$  contact spot. (b) Electron microscope image of fill tube stub with a larger contact spot.

## References for Section 12

- [12-1] A. Nikroo et al., *Fusion Sci. Technol.* **45**, 165 (2004).
- [12-2] J. Burmann, S. Letts, and M. Saculla, "One Piece Capsule/Fill Tube Assemblies," *Proc. 12th Target Fabrication Specialists Meeting*, Jackson Hole, Wyoming, 1998, p. 403.



### 13. 04CR/LA1 CRYOCONDENSATION APPARATUS FOR BERYLLIUM CAPSULES (N. ALEXANDER)

Task Leader: N.B. Alexander

In this task, we worked towards the realization of a deuterium prototype of the cryocondensation “Drill, Fill, and Plug” apparatus. The concept is shown in Fig. 15-4. This year we defined an optical interface and produced design drawings of the cryostat for review.

The design of the cryostat was further analyzed in ANSYS. In particular, we wanted to ensure that the window would not fog up. The window is being cooled through deuterium in the D<sub>2</sub> Space. In a typical controlled atmosphere of a laboratory the relative humidity is  $\leq 56\%$ . For the window not

to form condensation on it, its temperature needs to be above 286 K (55°F) when the relative humidity is up to 56%. The initial analysis indicated that the window would be too cold. Thickening the window did not completely solve the problem. The solution chosen was to add an annular heater to the window. This still allows light to pass through the center of the window and the model indicates that the heat loads to the cryocooler are still acceptable. Three watts of power are applied to the window heater. The model is shown in Fig. 13-1.

A more detailed sketch of the apparatus is shown in Fig. 13-2. A second copper spring has been added. This outer spring is used to provide additional cooling to the tip of the cone of the D<sub>2</sub> Space. This prevents the top of the capsule from getting too warm. The cone is made of gold plated fused silica to reduce heat load to the capsule. The final focus optics of the sealing laser will be outside of the cryostat window. The top level assembly drawing is shown in Fig. 13-3.

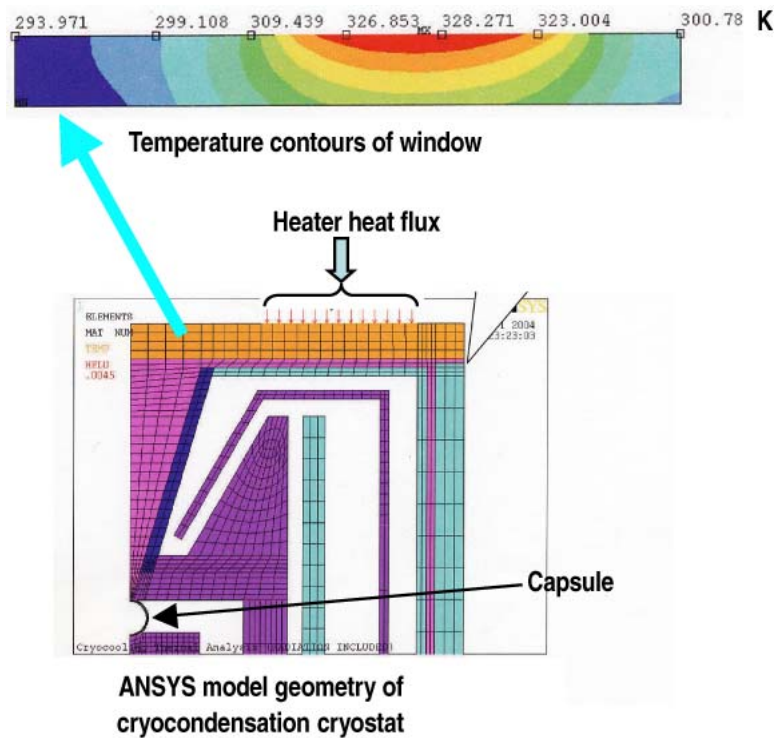


Fig. 13-1. A thermal model indicates that the window will be warm enough to prevent condensation (fogging) if an annular heater is added to the window.

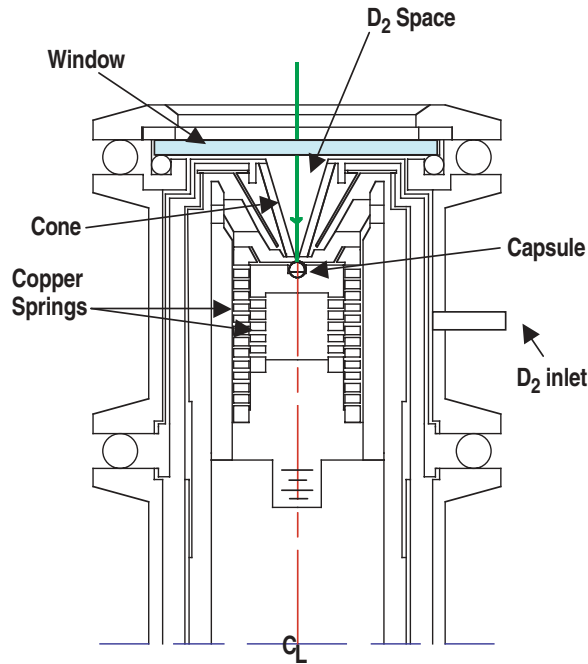


Fig. 13-2. The cryocondensation cryostat uses a second outer copper spring to cool the tip of the cone of the D<sub>2</sub> Space, so that the capsule is not over-heated.

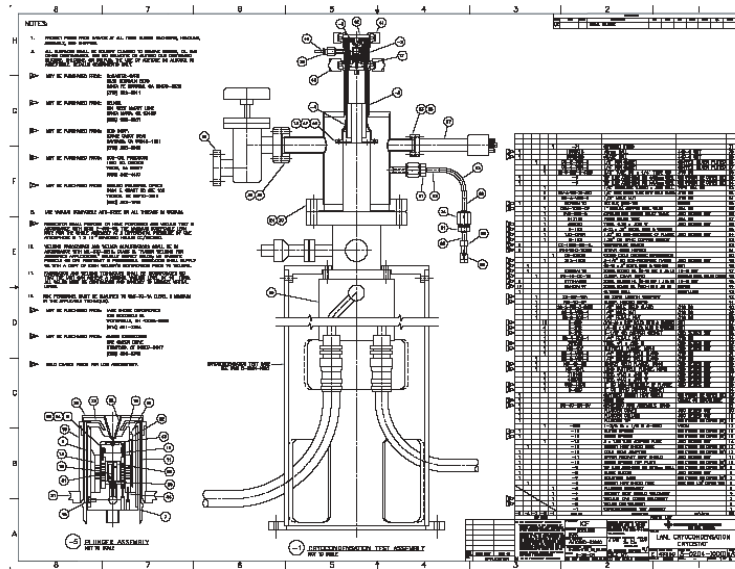


Fig. 13-3. The top level assembly drawing for the cryocondensation cryostat was prepared for review.

## 14. 04CR/LL1 ENHANCED CRYO TARGET FIELDING DEVELOPMENT (D. BITTNER)

Task Leader: D. Bittner

### 14.1. Slow Cooldown Experiments Under Low IR Power

The slow cooldown experiments continued this year. The goal of these experiments was to determine how low in temperature a layer could be cooled under low infrared (IR) power before significant layer degradation occurred. Solid deuterium layers were formed and cooled to between 1.0 and 1.5 K below the melting point under low IR power. Volumetric heating rates varied between 3 and  $6Q_{DT}$  ( $1Q_{DT} = 50 \text{ mW/cc}$ ) and the cooling rate ranged from 0.003 to 0.001 K/min. We tracked the layer degradation both visually and by calculating an rms value for the layer from each image.

Figure 14-1 contains a plot of the layer rms versus temperature relative to the melting point ( $T_{\text{melt}} - T$ ) for one of these experiments. The volumetric heating rate in this case was approximately  $3Q_{DT}$  and the cooling rate was 0.001 K/min. Each data point corresponds to an image capture during the slow cooldown process. Since layer roughening typically does not affect the first few modes, we calculated the rms value of the layer for modes 4 to 100. The rms values show some variation as the temperature was lowered to approximately 0.75 K below the melting point. Below 0.75 K the rms values sharply increase. Three images have also been inserted into the figure. At 0.18 K there were a few features apparent in the image. This was our reference image. Ideally all subsequent images would look like this one. However, by approximately 0.74 K a break was starting to appear in the brightband. Below 0.74 K noticeable changes started occurring in the layer. By 1.28 K there were more features in the image as well as multiple breaks in the brightband.

The data from these experiments indicate that layers can be slowly cooled to approximately 0.75 K below the triple point before significant layer degradation occurs. These results are consistent with previous measurements using  $D_2$  and earlier measurements in 1 mm o.d. capsules with hydrogen deuteride (HD).

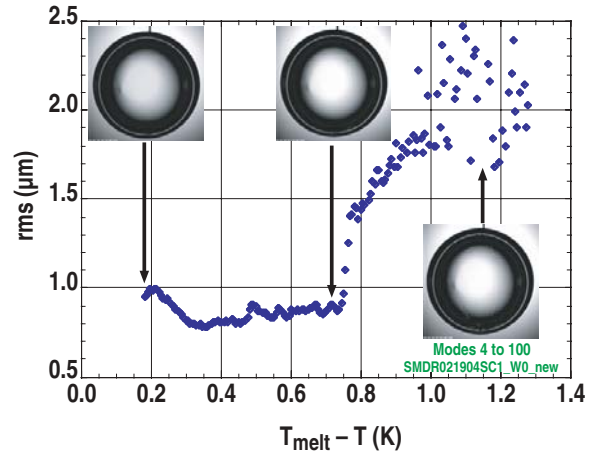


Fig. 14-1. Plot of the rms versus temperature for the slow cooldown of a solid deuterium layer under IR illumination. The IR illumination generated a volumetric heating of approximately  $3Q_{DT}$ . The rms values were calculated for modes 4 to 100.

### 14.2. Modeling of Cracks in Ice Layers

We have begun investigating the effects of ice layer cracks on our images. The layers formed and cooled at low IR power start to degrade before the temperature is lowered 1.5 K

below the triple point (see above). Typically this means that breaks form in the brightband. These breaks sometimes appear to be associated with features in the central region of the image, Fig. 14-2(a). There are qualitative indications that some of the features are due to discontinuities or linear fractures, such as cracks. These sorts of features are not properly analyzed by our layer analysis code. To investigate the effects of cracks in ice layers on our images, we performed a raytrace modeling survey of cracks. We modeled cracks of various sizes to start developing a general understanding of how the crack shape, size and aspect ratio impacts ice layer images.

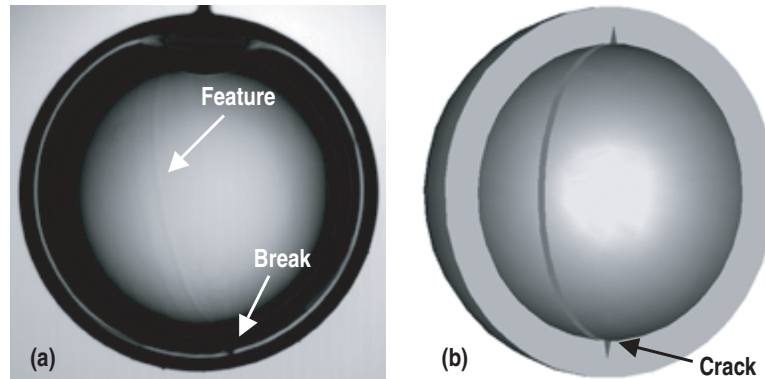


Fig. 14-2. (a) An image of an ice layer with a break in the brightband. (b) A cross-section of an ice layer showing a crack on the inner surface.

Most of our effort focused on cracks on the inner ice surface. The cracks were modeled as a torus with a triangular cross-section. Figure 14-2(b) shows the cross-section of an ice layer with a crack. This geometry gives one the ability to rotate the crack and thus be able to generate raytrace images of cracks at various angles. (All the raytrace models used parallel rays as the light source and a simple relay lens system to focus the rays onto a 512×512 array image plane.) These raytrace images of cracks look similar to images of layers after they have started to degrade. Whether or not a crack generated a break in the brightband was more dependent on the depth of the crack than its width. Figure 14-3 shows the raytrace image of a crack 3  $\mu\text{m}$  wide and 10  $\mu\text{m}$  deep and rotated 50° to the viewing axis. Notice the similarity between this raytrace image and the image in Fig. 14-2(a).

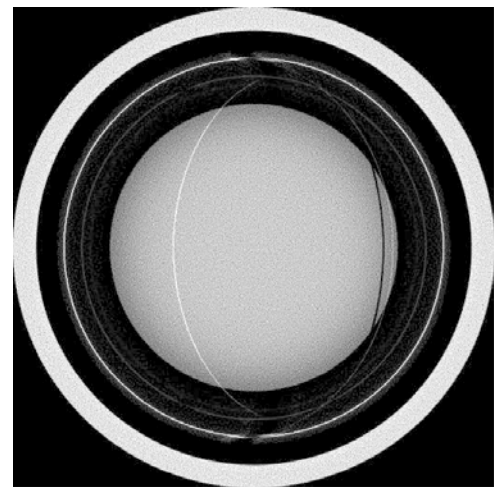


Fig. 14-3. Raytrace image of an ice layer with a 3  $\mu\text{m}$  wide by 10  $\mu\text{m}$  deep crack. The plane of the crack is rotated 50° to the viewing axis.

Once one determines a minimum size crack that would be a significant perturbation at ignition time, one can use our model to determine if cracks of that size are visible. Based on

estimates, cracks are expected to be significant if their cross-sectional area is greater than  $5 \mu\text{m}^2$  [14-1]. Using this value we have modeled various cracks with cross-sectional areas from 2.5 to  $5 \mu\text{m}^2$ . For all these cases, there were crack orientations that generated visible breaks in the brightband. There were also cases run with 1 and  $1.5 \mu\text{m}^2$  cross-section cracks. In these two cases the effect on the brightband was a small change in the brightband intensity. This initial modeling effort suggests that some breaks in the brightband may not indicate unacceptable layer degradation.

#### References for Section 14

[14-1] S. Haan, LLNL, private communication.



## 15. 04CR/NCTS NIF CRYO TARGET SYSTEM DEVELOPMENT AND ENGINEERING (N. ALEXANDER)

Task Leader: N.B. Alexander

This task revolved around two main areas. First, engineering and design activities for the Conceptual Design Report (CDR) for the NIF Cryogenic Target System (NCTS). Second, development and testing of the cryocondensation “drill, fill, and plug” concept for filling beryllium capsules with DT.

We participated in many NCTS engineering activities. We assembled and edited the “NCTS Pre-CDR Description”. We coauthored target assembly design definition documents [15-1,15-2] and began an interface document between the target and the NCTS. We prepared an initial cost estimate for the NCTS. We helped develop the requirements table for the NCTS. We worked on the NCTS shot cycle. This developed a list of operation steps to field the target and estimated times for these operations. Various target design fill pressures were calculated. We presented the Fill System Design at the Initial Concept Review for the NCTS. We began investigation of a number of advanced concepts for the NCTS. These included one-sided shroud retraction and low vibration cryocoolers.

The ignition targets will be kept layered and cryogenic inside of a shroud mounted on the end of the ignition-target inserter and cryostat (I-TIC). The shroud must be removed from around the target just before the target is illuminated with the NIF laser beams. The one-sided shroud retraction concept we conceived is shown in Fig. 15-1. Linear motors inside of the I-TIC pull the shroud back towards the base of the I-TIC. There is a small hole in the shroud so that the target is free to protrude out of the shroud when the shroud is pulled. To keep helium in the shroud, prior to shroud pulling, a very thin polyimide window is placed over the hole in the shroud. The helium is used to transport heat out of the direct drive target to the shroud. An

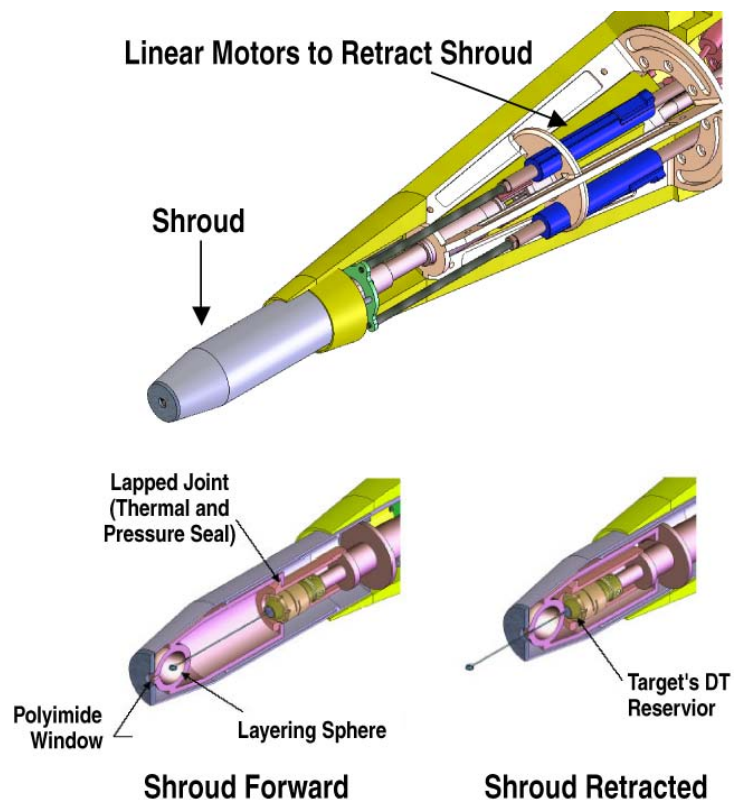


Fig. 15-1. Axial one-sided shroud retraction concept. The polyimide window holds in helium. It is broken by a ~8 Torr pressure pulse just before the shroud is retracted.

indirect drive target would not use this helium so the film would not be needed in this case. Heat is removed from the shroud through a bare lapped thermal joint. This allows the shroud to be retracted freely. The film is broken just before the shroud is pulled so that the film doesn't damage the target during shroud retraction. This can be done by mechanical means or by means of a very small pressure pulse ( $\sim 8$  Torr) in the helium in the shroud. A one-sided shroud retractor would save the NCTS the cost of an opposed port shroud retractor. This is a device that reaches into the NIF target chamber from the opposite port that the I-TIC is installed in. It pulls the shroud completely off of the I-TIC in the direction away from the I-TIC.

A mechanical cryocooler, Gifford-McMahon type, is being considered for cooling the I-TIC. This leads to the possibility of vibrations of the cryocooler inducing unacceptably large vibrations in the target mount. The current requirement is that the target be held in position to within  $\pm 6.8 \mu\text{m}$ . There are several options to reduce vibrations. Use a different type of cryocooler. These could be based on multi-stage Joule-Thompson cycle or a turbo-Brayton cycle. Both would have to be developed. The former cools by expanding gas through nozzles, so has no moving parts. The later expands gas through a rotary turbine. With the moving part being a rotary rather than the linear piston movement of the Gifford-McMahon, the vibration will be reduced. Another option is to use an active vibration cancellation system. In this system, sensors measure the vibration of the cryocooler and a control system moves a set of mechanical actuators holding the cryocooler in a fashion that cancels the vibrations transmitted through the base of the actuators to the rest of the I-TIC. The cryocooler heat removal stations then have to have a low stiffness thermal connection to the I-TIC. This can be accomplished in the manner of a gas gap heat switch with the switch housing containing a metal bellows for low stiffness. Realizations of this type of vibration reduction system have been reported in the literature for small Stirling cycle cryocooler connected to hexapod motion actuators. Another option is to turn off the cryocooler prior to the shot and also potentially during characterization of the target by phase contrast x-ray imaging. The time that the target must stay cold after the cryocooler has been turned off may be minutes to tens of minutes. This allows for characterization and potentially pre-shot alignment of the beams to the target. To allow these time scales, a high heat capacity heat sink has to be added to the I-TIC. One way to do this is to add a liquid helium pot as the heat sink and use a 4 K cryocooler. This is illustrated in Fig. 15-2. The system is closed; no external liquid helium is added. The cryocooler liquefies helium from the buffer tank and helium exhaust from the pot is returned to the buffer tank.

Designers worked with LLNL and our engineers to model many concepts of NCTS systems. These include a cryocooler-based I-TIC, a TIC Transporter used to house the I-TICs just in the NIF building, a side-mounted indirect drive shroud, a Layering and Characterization Station, and a direct drive fill station. Some of these models are shown in Fig. 15-3. Exploded view drawings were made from some of these models to aid in the costing of the NCTS.

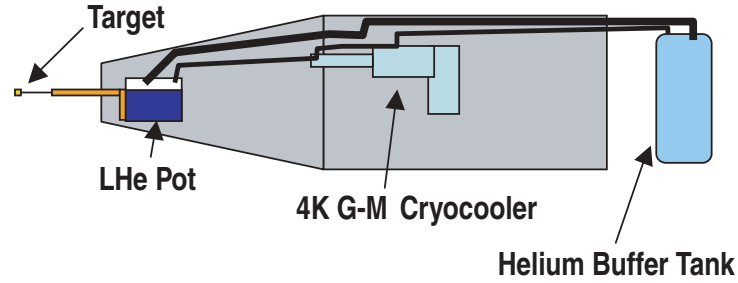


Fig. 15-2. This concept allows the cryocooler to be turned off before the shot, reducing vibration of the target. Since a 4 K cryocooler is used, no external liquid helium is used.

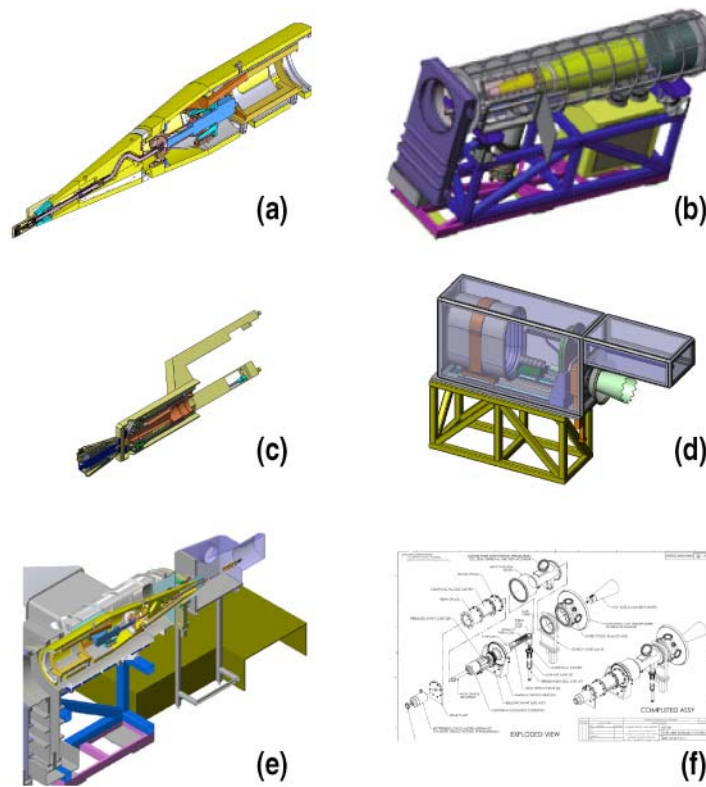


Fig. 15-3. Models were made of concepts of many NCTS systems. (a) I-TIC, (b) TIC Transporter, (c) indirect drive shroud, (d) direct drive fill station, (e) layering and characterization station, (f) exploded view drawing for costing.

The cryocondensation Drill, Fill, and Plug concept is a method for sealing DT, or other gases, into beryllium capsules. High fill densities are obtained using low temperature ( $\leq 300$  K) and low pressures ( $\leq 1$  atm). Ideally, this would be used to fill capsules with up to as much fill gas as they could hold in without breaking at room temperature. The target could then be assembled around a filled capsule, and warm-loaded into the I-TIC for fielding on the NIF.

The concept is illustrated in Fig. 15-4. To start, a capsule is laser drilled with a small hole on top ( $\sim 5 \mu\text{m}$ ). The capsule is placed on top of cryocooler with a copper spring. A windowed vacuum can is placed over the capsule and cryocooler. A cone in the vacuum can seals to the capsule to provide separate spaces to place DT above the capsule and below to vacuum insulate the cryocooler. The copper spring provides both a cooling path from the capsule to the cryocooler and compliance to the cone of the vacuum can, so that the capsule is not crushed during assembly. The capsule is cooled. The DT fuel is condensed into the capsule from the DT Space. When sufficient fuel is in the capsule a laser pulse is sent through the window to seal shut the hole. The fill is determined by differential pressure, temperature, volume measurements on the DT Space above the capsule.

The detail of the thermal model of this concept was increased. We examined the effect of different thickness of grease at the thermal interfaces of the apparatus. The ANSYS code was used to model the apparatus, see Fig. 15-5. The heat load to cryocooler was found to be insensitive to the grease thickness; 0.54 W to the first stage, 0.32 W to the second stage. These head loads can be handled by a small cryocooler. The capsule could also be held cold enough to condense fuel at the bottom and warm enough at the top to prevent liquid formation in the capsule's hole for a wide range of grease thicknesses.

The grease seal between the capsule and the cone was tested at room and liquid nitrogen temperatures. A sketch of the core of the apparatus is shown in Fig. 15-6, along with the picture of the steel ball bearing (a surrogate for a beryllium capsule) after it had been removed from the test apparatus. The apparatus shown was immersed in a Dewar of liquid nitrogen for the liquid nitrogen temperature tests (77 K). The ball bearing pictures show the ring of grease left behind after removal from the apparatus. Importantly, the grease did not smear into the top circular region where the hole in a capsule would be located. The surfaces touching the capsule were pre-dimpled with a slightly larger ball bearing to provide a smooth spherical surface for the capsule to contact. This provides good sealing at the top and good thermal contact at the bottom. No leak was observed 15 psi helium applied, using a helium leak detector set to the  $10^{-8}$  scale. This is at both room temperature and liquid nitrogen temperature, and using spring forces of 1.14 $\times$ , 1.19 $\times$ , 1.61 $\times$ , and 1.72 $\times$  the nominal spring design force.

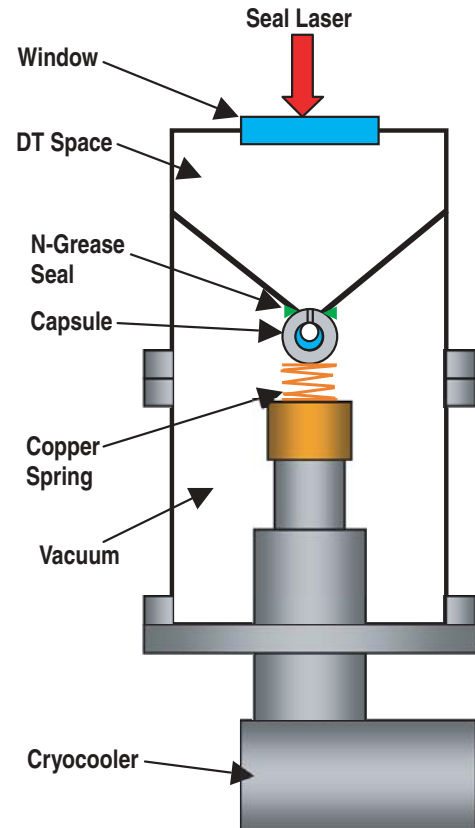


Fig. 15-4. The cryocondensation “drill, fill, and plug” concept uses cryogenic temperatures to condense a high density of DT into a beryllium capsule through a small hole. The capsule hole is then sealed shut with a laser.

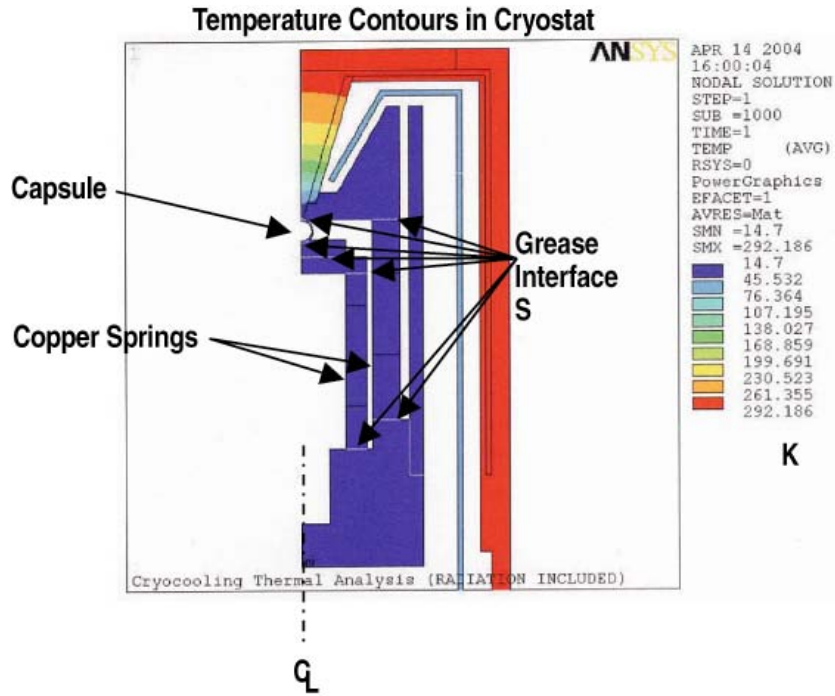


Fig. 15-5. Thermal model indicates that the capsule can be cooled to condense DT with heat loads that can be accommodated by a small cryocooler.

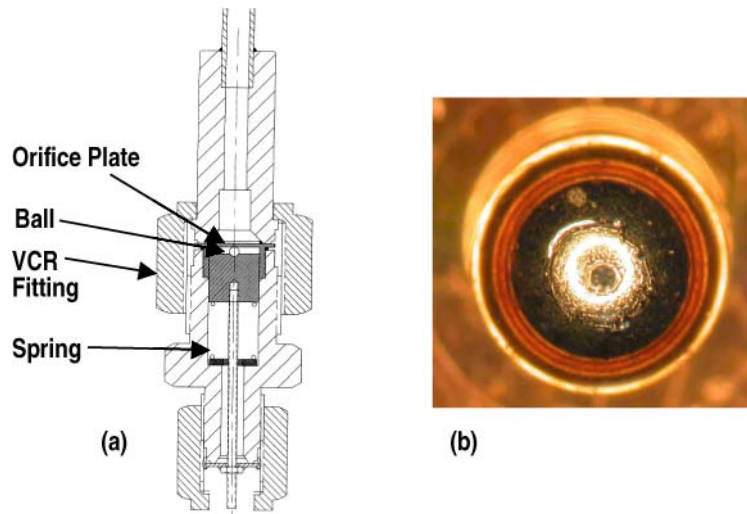


Fig. 15-6. (a) Apparatus for testing capsule to cone seal down to 77 K. (b) Grease on top of ball removed from apparatus; no grease observed in top circle where capsule hole would be.

To test the grease seal at cryogenic temperatures of 10 to 20 K, an apparatus was designed and mostly assembled, see Fig. 15-7. It is based on a cryocooler, with many similarities to the cryocondensation concept apparatus. This includes the copper spring. The

apparatus also has windows. These will allow the capsule to be replaced with a miniature see-through vial. This will be used to test the condensation into a small region through a micro-hole, with visual confirmation of the fill condensate. The concept for the vial is shown in Fig. 15-8. The sides of the vial's Invar frame is sized so that the vial has a similar thermal conductance as a beryllium capsule.



Fig. 15-7. Apparatus for testing capsule to cone seal at 10 to 20 K.

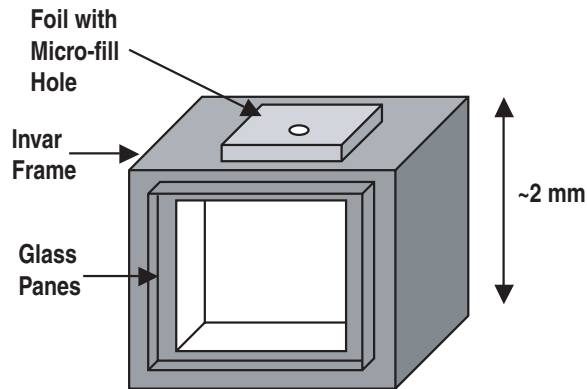


Fig. 15-8. Concept for a miniature see-through vial to replace capsule. This allows visual confirmation of condensate fill through micro-hole.

**References for Section 15**

- [15-1] Indirect Drive Warm-Loaded Ignition Target Design, UCRL-TR-206424.
- [15-2] Indirect Drive Cold-Loaded Ignition Target Design, UCRL-TR-206426.

## 16. 04NIF/CD NIF CAPSULE DEVELOPMENT (A. NIKROO)

### 16.1. NIF/CD Evaluation of Ge-doped CH/CD Ablator

The following is a report on the preliminary evaluation of fabrication of full thickness Ge-doped CH shells for the National Ignition Facility (NIF). We briefly discuss the method of fabrication and then report on the current status and unresolved issues with production of such shells based on the work performed in FY04. In particular, we discuss the evaluation of the surface finish of full thickness CH shells, which was the topic of emphasis in FY04.

#### 16.1.1. Fabrication Technique

The Ge-doped CH/CD ablator material is produced by chemical vapor deposition of a polymer in vacuum plasma. This process is commonly referred to as plasma polymerization and was first developed for ICF target fabrication over twenty years ago [16-1]. In this process, in its most basic form, a hydrocarbon gas, the precursor, is broken down in an inductively coupled plasma system. The fragments deposit on the substrates and form a pure CH polymer film. The addition of excess hydrogen gas to the process is essential in obtaining smooth, virtually stress-free films at the thicknesses required for ICF laser implosions (tens to over a hundred microns). Deuterated films (CD) are obtained by changing the precursor hydrocarbon gas to its fully deuterated analog (as well as using D<sub>2</sub> instead of hydrogen). Incorporation of dopants is achieved by adding a precursor gas or vapor containing the desired dopant atom. For example, for germanium, the vapor of tetramethyl germanium (TMG) is added to the basic process used for undoped coatings [16-2]. The relative concentration of TMG in the process controls the level of doping. The coating rate is rather slow, only about 0.3-0.5  $\mu\text{m}/\text{h}$ , requiring over two weeks to deposit the full NIF thickness of  $\sim 150 \mu\text{m}$ .

Ge-doped CH is deposited on high quality shells, referred to as mandrels, of appropriate diameter to produce the desired spherical NIF target. The mandrel is typically poly- $\alpha$ -methylstyrene (PAMS) which is produced by microencapsulation [16-3]. This mandrel may be thermally removed subsequent to the coating operation. Uniform coating of mandrels requires agitation during deposition of the Ge-doped CH coating. Typically mandrels are placed in a pan attached to a piezo electric shaker to provide this required agitation during coating. However, for NIF size shells ( $\sim 2 \text{ mm}$  diameter) another agitation scheme is used where the coating pan is tapped every few minutes during the coating [16-4]. This avoids the agitation-induced defects observed when the piezo shaking technique is used. Typically 10 mandrels can be coated in a single coating run.

The fabricated shells are characterized by a variety of techniques including microscopy, white light interferometry and the atomic force microscope (AFM) spheremapper. The AFM spheremapper, in particular, is considered to provide the most important metrology data and is typically used to evaluate the quality of the shell. The AFM spheremapper produced power spectra of the shells are compared to the desired spectrum, "the NIF standard", provided by current designs. The AFM spheremaps are generally performed by mapping the shell in three

closely spaced traces about three orthogonal axes. This operation can be performed in about 30 minutes. The “full spheremap” technique (70 traces in each of 5 axes) allows much more detailed examination of the surface, especially in high modes, but the operation is much more time consuming, typically requiring 5 h per shell. We mainly used the standard AFM spheremapping and reserved the “full spheremap” for the best shells.

### 16.1.2. Surface Finish

In FY04, our evaluation was focused on examining pure CH coatings. Previous data on Ge-doped CH coatings indicate that the surface finish for the two materials evolves very similarly. So, the information obtained on CH coatings is very much pertinent. In FY04, full thickness CH shells were produced routinely as described above. We found no major issues in producing the full thickness, such as coater, agitation or other system failures during the long coatings. We were able to produce shells, which had AFM power spectra near or below the “NIF standard” as shown in Fig. 16-1. Such results were not consistently reproduced and typically fewer than 10% of shells in any given batch were near the “NIF standard”. The major defects on full thickness CH shells that resulted in excess power in the modal spectra above the “NIF standard” were isolated dome-like features. Identification of the sources of such isolated features made up the majority of the latter part of our work in FY04.

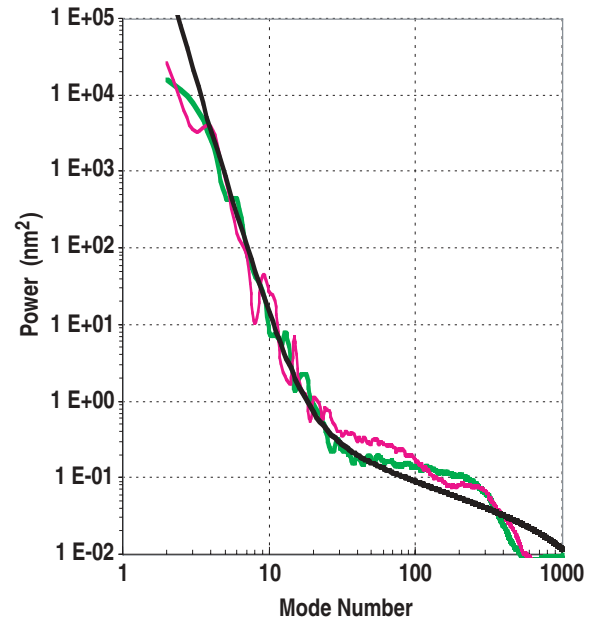


Fig. 16-1. Full thickness CH shells very nearly meeting the “NIF standard” were produced in FY04 using plasma polymerization coating technique. The yield of such shells, however, has been low (~10%) due to the presence of large isolated features on the shells.

In general, there are several possible reasons for the surface finish of the full thickness shells not meeting the NIF standard. The most obvious is the plasma polymer coating process itself. The second is the quality of the mandrel. Any low mode features on the mandrel will be reproduced on the final shell. Also, any high mode roughness or isolated defects present on the mandrels grow during the coating and degrade the surface finish of the full thickness shell. The third is any isolated defects produced during the coating due to agitation as observed on thinner coatings on 2 mm diameter mandrels previously. Finally, there is always the issue of cleanliness of the process in each of its steps. We examined each of these possibilities as part of our evaluation as discussed in the following.

The coating process itself had been previously examined numerous times on thick coatings on flat substrates, as well as coatings on smaller shells (~1 mm diameter) [16-5]. These examinations had indicated that the coating process is inherently suitable for ICF

target fabrication, yielding RMS surface finish of a few nm for coatings over  $100\ \mu\text{m}$  thick, consistent with the “NIF standard” requirement. The surface finish here refers to the ubiquitous background finish, ignoring any isolated features on the surface. It is usually measured by coating on ultra-smooth surfaces such as freshly cleaved mica. Coating on such ultra-smooth surfaces also indicates that the coating process itself does not generate any isolated defects such as dome-like structures. However, fine tuning of the coating parameters is required for a given plasma polymer coater to obtain the desired surface finish. Such optimization was carried out on the coater designated for this work to obtain thick coatings with the desired few nm RMS background surface finish without presence of any isolated domes. Indeed the background surface finish on full thickness shells produced throughout our evaluation was as desired.

The other causes of surface degradation mainly have to do with isolated features in the form of domes. As mentioned above, this is the main issue remaining with fabrication of “NIF quality” full thickness CH shells *routinely*. The AFM surface profile shown in Fig. 16-2 illustrates this problem. The majority of these domes are typically a few microns wide and a few tenths of microns tall. These smaller domes, in general, do not degrade the power spectrum significantly. However, larger domes, mainly those  $\sim 1\ \mu\text{m}$  in height or taller, while much

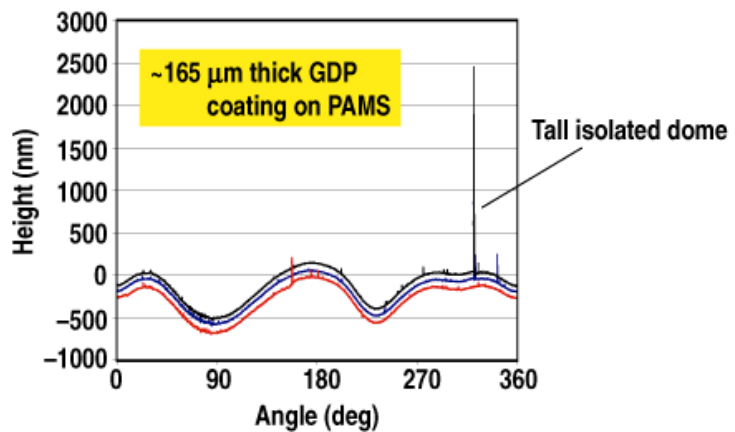


Fig. 16-2. The surface height deviation as a function of angle as mapped by the AFM spheremapper. The major cause of excess power in the modal spectrum of full thickness CH shells is the large spike (at  $\sim 300$  deg) in the AFM trace as shown in the figure. The spike is due to an isolated dome. Note also the smaller spikes corresponding to domes only a few tenths of a micron tall. These features do not significantly affect the power spectrum.

lower in density, do lead to significant increase in the power spectrum well beyond the NIF standard. Two of the possible causes of dome generation, large or small, are (1) seeds on the mandrels introduced in their fabrication and (2) possible agitation induced defects during coating. It is well known that the quality of the mandrels used for coatings is batch dependent. Also, agitation during coating has been shown to induce such defects [16-4]. While it is difficult to separate these two causes, we attempted to do that in a systematic fashion and showed that the agitation during the coating process is not the major cause of dome generation.

In the initial part of our systematic examination of the process, we examined dozens of mandrel batches using shorter ( $\sim 6$ - $7$  day,  $\sim 70\ \mu\text{m}$  thickness) coating runs. Only mandrels from those batches with shells consistently meeting the “NIF standard” were used for coatings. To distinguish between mandrel defects and possible agitation induced defects, mandrels from several different batches were coated in the *same* coating run. The fact that

shells from some batches produced poorer surfaces than others indicated a problem with that particular batch. Through this culling process we were able to identify several batches as being superior to others and only those were used in any further work. To further separate the cause of dome generation, coated shells from the remaining batches were coated for another week reaching full thickness. The number of domes detected after one and then two weeks of coating were counted and compared. Only a slight increase in the number of domes was observed in doubling the thickness, indicating the coating process was not the main source of dome generation. In addition, coatings of fixed mandrels, i.e., those coated *without* any agitation, also showed growth of domes from the mandrel surface. It was concluded from these results that the majority of isolated features were produced from seeds present on the mandrel. However, most of these domes were in the few tenths of microns and we could not explain the presence of taller domes from this examination.

We are currently investigating the possibility that lack of clean handling of shells prior and post coating may be the major source of such taller domes. Post coating debris is easily distinguished from those present prior to coating, as they are free to move on the surface and also can be detected optically as loose debris. Also, in general, shells are handled much more cleanly after the coating prior to AFM examination. Most of the tall domes we have observed are firmly attached to the shell surface and therefore were present prior to coating. The lack of thorough clean handling in our process has been dictated by the necessity of examining mandrels carefully prior to coating. This has been necessary as a significant percentage of mandrels contain middle mode defects that are reproduced in the fully coated shell. We have begun bypassing this step in the interest of cleanliness to determine if that avoids large dome formation on the final shells. Our most recent results seem to confirm this as the high mode roughness is small on the majority of shells coated this way as seen in Fig. 16-3. The presence of the large middle mode power in one of the spectra shown is the direct result of not examining the mandrels prior to coating. In addition, we have performed a “full spheremap” of these shells and compared to the best obtained with standard handling. This is shown in Fig. 16-4. The number of large spikes seen in the expanded surface scale is significantly fewer in the case of clean handling. We are in the process of procuring an appropriate microscope for our cleanroom in which the mandrels are made to be able to keep the shells in a cleanroom environment throughout their journey into the coater.

## References for Section 16

- [16-1] S.A. Letts, D.W. Myers, L.A. Witt, J. Vac. Sci. Technol. **19**, 739 (1981).
- [16-2] R. Brusasco, M. Saculla, R. Cook, J. Vac. Sci. Technol. A Vac. Surf. Films. **13**, 948 (1995).
- [16-3] M. Takagi, R. Cook, B. McQuillan, et al., Fusion Sci. Technol. **41** 278 (2002).
- [16-4] A. Nikroo, D. Woodhouse, “Bounce coating induced domes on glow discharge polymer coated shells,” 12th Target Fabrication Specialists Meeting, Jackson Hole, Wyoming, 1998; Fusion Technol. **35**, 202 (1999).

- [16-5] A. Nikroo, J. Pontelandolfo, E. Castillo, “Coating and Mandrel Effects on Fabrication of Glow Discharge Polymer NIF Scale Indirect Drive Capsules,” 14th Target Fabrication Meeting, West Point, New York, 2001, to be published in Fusion Sci. Technol. (2002).

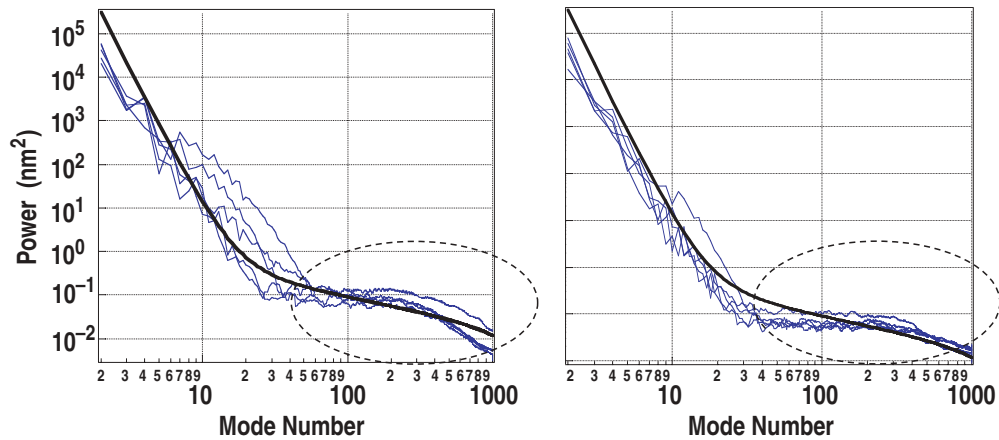


Fig. 16-3. Examples of AFM power spectra of full thickness pure CH shells made using complete clean handling. The high modes for over 50% of shells were at or near the NIF curve. The middle mode power in one of the shells is the result of not pre-selecting the mandrels for coating (to avoid particulate pick up during selection in a non-clean environment). The high modes which are directly affected by the coating process are very near the NIF standard.

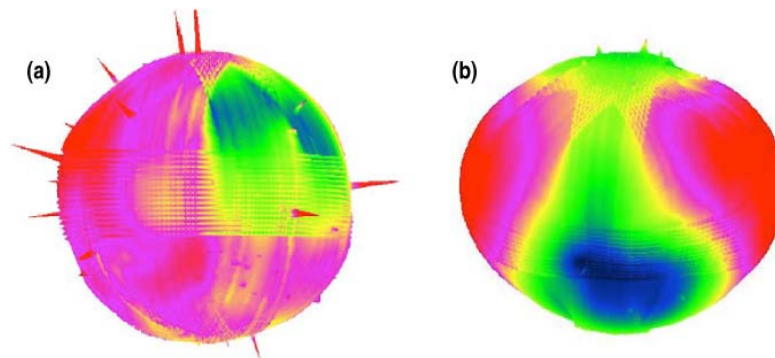


Fig. 16-4. (a) “Full spheremap” of one of the shells having a three-axis spheremap spectrum meeting the NIF standard produced not using complete clean handling produced earlier in FY04. Note the large spikes detected with a more thorough examination in the “full spheremap”. The scale is expanded by 300x in the radial direction. (b) “Full spheremap” of one of the shells having a three-axis spheremap spectrum meeting the NIF standard produced using complete clean handling produced recently. The number of large spikes has been substantially reduced. The scale is expanded by 300x in the radial direction.



## 17. 04CAP-1 CAPABILITIES IMPROVEMENT (A. NIKROO)

### 17.1. Glass Permeation Barrier Target Fabrication and Characterization

Thin sputtered glass layers have been explored as a permeation barrier. This method was used to replace polyvinyl alcohol (PVA) as a permeation barrier. PVA's low yield and relatively large (2-4  $\mu\text{m}$ ) nonuniformity make it undesirable for NIF- and SNL-size capsules (greater than 2 mm o.d.). More importantly, the room-temperature DD half-life of PVA-coated shells is generally less than 1 week. The half-life of glass-coated shells is expected to be greater than 4 weeks. The development of sputtered glass as a permeation barrier and the novel use of mass spectrometry to measure the permeability through these shells were initiated in FY04.

The glass layer was deposited on the mandrels in an RF sputtering system, with high-purity quartz as the sputtering target. Typically, plasma polymer shells  $\sim$ 2 mm diameter with  $\sim$ 30  $\mu\text{m}$  wall thickness were used as the starting mandrels. The mandrels are placed in an agitation pan to randomize their orientation to produce a uniform coating. The coating parameters investigated were the argon pressure during sputtering, the number of shells in a coating batch, and the agitation method of the shells. Sputter-coatings were performed at 2, 5, and 10 mTorr of argon pressure. The agitation methods were gently bouncing the shells in a piezoelectric vibrating pan, or rolling the shells in a rotating pan.

The sputter-coated shells were analyzed by optical microscope to inspect for cracks and general surface quality. The surfaces were also compared to the original surface smoothness of the mandrels. Scanning electron microscopy (SEM) was used to visualize surfaces at higher magnification. Glass thicknesses were determined by interference microscopy. Wall thickness variations were measured on an adapted Filmetrics spectral interferometer which traced wall thickness about the shell's equator. The permeation half-life was measured on a novel mass spectrometer-based system.

The design of the mass-spectrometer system to measure permeation is critical to the development of permeation barrier targets. The system allows the permeability of shells with a long half-life to be measured quickly. The spherical targets to be measured are first permeation-filled in a pressure cell. The measurement apparatus consists of small volume attached to a mass spectrometer residual gas analyzer. Construction was designed to minimize the internal volume of the system. To measure the permeability, a gas-filled shell is placed in a small evacuated volume, and then exposed to the gas analyzer. The ion current resulting from the permeating gas is recorded. The slope of the ion current is used directly (for very permeable shells) or the magnitude of the ion current is compared against that of a shell with well-known permeability (for low-permeability shells) to generate the unknown shell's permeability and half-life.

A full report on the progress of glass permeation barrier targets and development of the mass spectrometer permeation measurement system will be reported in the FY05 annual report.

## 17.2. 3D Surface Reconstruction of ICF Shells after Full Surface Spheremapping

**Introduction.** Rayleigh-Taylor (RT) instability mandates very stringent surface finishing requirement on ICF shells [17-1]–[17-3]. Surface characterization techniques have not been adequate to satisfy these specifications. The workhorse spheremapper instrument can measure surface roughness with nanometer resolution and can detect long wavelength distortion very well. However, the limited actuator range only allows measurement within a very narrow orbit ( $\sim 80 \mu\text{m}$ ) around the equator. This leaves the user to wonder what defects are missed by the trace measurements and what the shell looks like in three dimensions (Fig. 17-1).

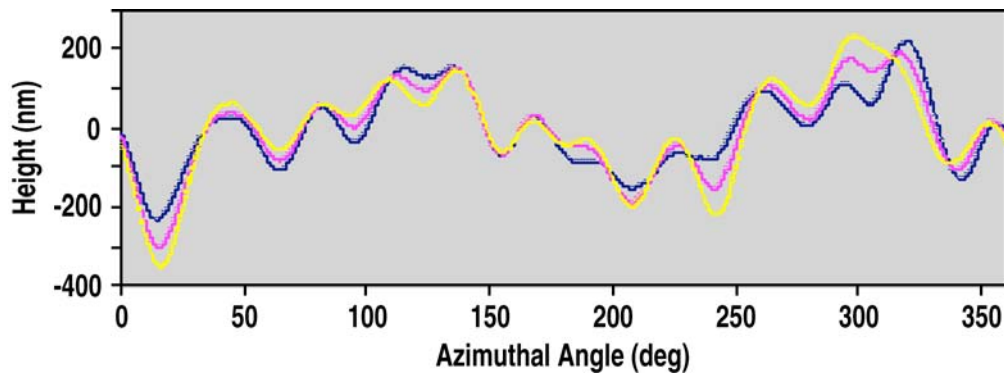


Fig. 17-1. Three spheremapper traces  $40 \mu\text{m}$  apart near the equator of a NIF-sized shell. The orbit is  $80 \mu\text{m}$  wide, close to the maximum possible before spheremapper hardware upgrade.

The first piece of the puzzle is solved with a spheremapper hardware upgrade, which allows  $640 \mu\text{m}$  wide orbit to be measured on a NIF-sized shell. Five such orbits cover over 95% of the shell surface. No defect of lateral dimension larger than the trace spacing goes undetected within each orbit [17-4].

3D surface reconstruction, however, is far from a display problem shown in 2D with the assumption that all traces have the same radius. Spheremapper only measures the height variation, but not the height itself. Mode 0 (average radius) is inherently missing and not necessarily invariant from trace to trace. Mode 1 is partly due to shell misalignment about the rotation axis and partly due to shell distortion. Slight thermal drift, inaccuracy in shell reorientation from orbit to orbit, and imperfection in AFM traces further complicates the problem. As a result, mode 0, mode 1 and some higher mode information must be retrieved for each trace before they are coherent with each other on a nanometer scale. We have developed a mathematical algorithm to reconstruct the entire ICF shell surface to 10 nm accuracy, from which the  $R(\theta, \phi)$  map with 1 deg angular resolution can be constructed.

### 3D Reconstruction Method

Figure 17-2 visually illustrates the processing flow. Figure 17-2(a) is a straight display of trace data with all artifacts removed. It is apparent that the measured radius is multi-valued on a nanometer scale for reasons discussed earlier. Our approach is to retrieve the missing information by systematically minimizing the height difference at trace intersections. We

define the new optimized trace  $R^i(\theta)$  as the sum of the measured trace  $H^i(\theta)$ , the nominal shell radius  $R_0$  (which is trace independent), and the mode correction terms to be determined.

$$R^i(\theta) = H^i(\theta) + R_0 + A_0^i + \sum_{k=1}^{km} [A_k^i \sin(k\theta) + B_k^i \cos(k\theta)] \quad , \quad (17-1)$$

where  $i$  is the trace index and  $k$  is the mode index.  $A_0^i$  is the mode 0 correction for trace  $i$ . All higher-mode corrections have two orthogonal components, with amplitudes specified by  $A_k^i$  and  $B_k^i$ . The mode coefficients are the unknown variables to be solved through an iterative process during which traces from one orbit at a time is held constant while the intersecting traces are adjusted. The convergence is quick and unique; with the traces closely retaining the original shape.

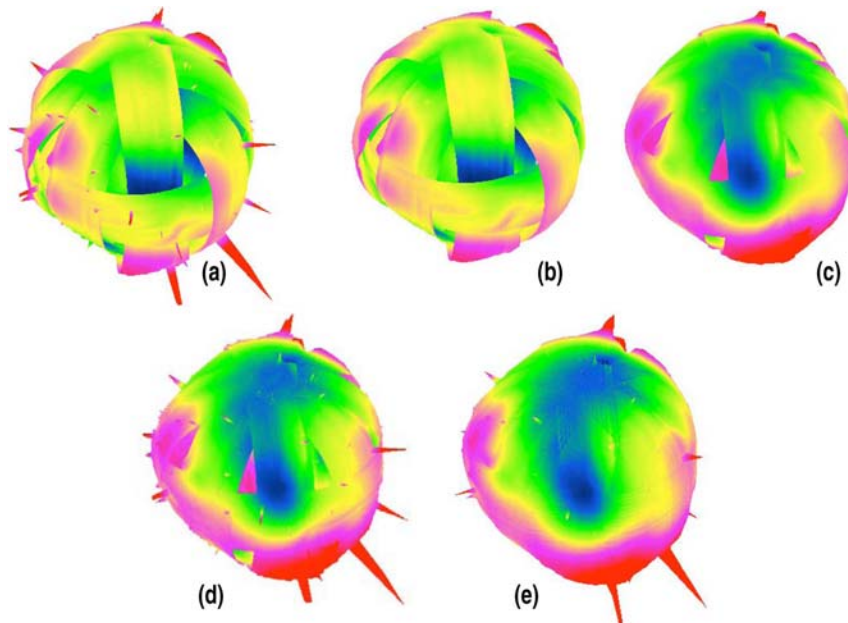


Fig. 17-2. 3D visualization of the process flow steps with all distortions magnified 300x. (The tallest defect  $2.5 \mu\text{m}$  in height.) (a) Step #1: 3D Display of artifact-free data showing the intrinsic incoherency of spheremapper traces. (b) Step #2: All sharp features temporarily removed. (c) Step #3: Low-mode surface optimized by minimizing height difference at trace intersections. (d) Step #5: The difference ( $\#4 = \#3 - \#2$ ) is added back to each trace ( $\#1$ ) to produce low-mode optimized surface with all the point defects ( $\#5 = \#1 + \#4$ ). (e) Step #6:  $R(\theta, \phi)$  map is produced by averaging to one radius per angular coordinate with  $1^\circ$  resolution and by extrapolating in small non-covered regions.

The angle misalignment has serious implications to the optimization procedures: If a point defect is picked up by one trace but not the other at an intersection, it does not make sense trying to minimize the height difference. Therefore it is necessary to temporarily remove all point defects, as shown in Fig. 17-2(b) (Step #2 in the process flow) before performing the calculation which yields the low-mode corrected traces, as shown in Fig. 17-2(c)

(Step #3). The change in each trace is captured in a difference file ( $\#4 = \#3 - \#2$ ), which is added back to Fig. 17-2(a) (Step #1) to produce the low-mode optimized surface that retained all point defects, as shown in Fig. 17-2(d) (Step #5 =  $\#1 + \#4$ ). We then produce the  $R(\theta, \phi)$  map by averaging to one radius per 1 deg angular coordinate and by extrapolating into small non-covered regions, as shown in Fig. 17-2(e) (Step #6).

The most important application of the  $R(\theta, \phi)$  map is target implosion simulation. The map can be used as realistic input conditions for the Hydro simulation code to predict the target performance prior to a shot, with the simulated result compared against the actual target performance to further our understanding on implosion physics. The  $R(\theta, \phi)$  map also provides characterization feedback to the production engineer for process feedback. As an example, the shell in Fig. 17-1 is 3D reconstructed to 5 nm accuracy in Fig. 17-3. The shell has a pronounced mode 2 distortion that hides the extent of the mid-mode pattern. When modes  $<6$  are removed, the mid-mode Marangoni pattern becomes conspicuous. These surface patterns are caused by within-the-wall convection cells formed during the PAMS drying process [17-5, 17-6]. The amplitude is intimately linked to the process conditions and can be completely tuned out through process optimization.

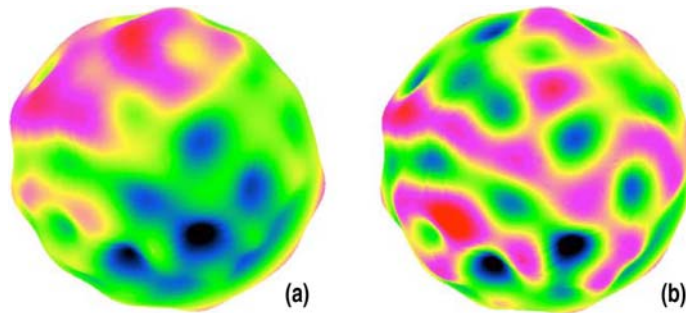


Fig. 17-3. PAMS shell surface reconstructed to 5 nm accuracy showing distinctive mid-mode process defects (distortion magnified by 300x). (a) All modes. (b) Mode 5 and below removed.

Our current focus is to reduce the angular uncertainty in shell repositioning through hardware improvement. If the wobble when releasing a shell can be reduced from 3-5 deg to 2 deg, we expect the reconstruction accuracy to be routinely controlled to 5 nm. We plan to use machine vision to provide the feedback and motorized stages to deliver the shell to the precise xyz location.

### 17.3. In-situ Ultrasonic Witness Plate Measurements

Witness plates made of different materials and ranging in thicknesses from 10  $\mu\text{m}$  up to 100  $\mu\text{m}$  and with a surface finish of better than 100 $\text{\AA}$  rms are used for diagnostics in ICF experiments. To achieve the desired thickness and surface finish these witness plates are fabricated by diamond turning. Occasional shifts in tool position can occur during diamond turning as a result of temperature fluctuations, tool wear, and part positioning can cause variations in the thickness of the witness plates, resulting in witness plates that do not meet

the thickness specifications. Ultrasound was identified as a potential technique that could be used for process monitoring and to catch any thickness variations before too much time and effort is invested in making the witness plates. Ultrasound provides a non-destructive measurement and can be done in-situ and without interfering with the diamond turning equipment.

A submicron resolution ultrasonic thickness measurement system made by GE Panametrics was identified as a system that could be used to monitor thickness of diamond turned parts. The GE Panametrics TGM System has a thickness resolution of  $0.25\ \mu\text{m}$  and can measure thicknesses down to  $10\ \mu\text{m}$ . To validate the TGM System thickness, measurements were done by GE Panametrics on a diamond turned aluminum plate, provided by GA, with two circumferential steps  $100$  and  $200\ \mu\text{m}$  high. The ultrasound thickness measurements were collaborated with thickness measurements done at GA via three point optical interference fringes measurements. Initial results indicate that the ultrasound measurements were within  $\pm 3\ \mu\text{m}$  of the optical interference measurements after correcting for phase shift. The need for a phase shift correction was attributed to a possible error in the selection of the starting point for either the ultrasound or optical interference measurements. The results are very encouraging and show that ultrasound gauging can be a technique that can be implemented in the fabrication of ICF components. In FY05, this effort will continue and will investigate the minimum thickness that can be successfully measured with the TGM System, and verify that the phase correction was a result of an error in the measurements starting point, as well as investigate the effects of glue joint on the shape of the backwall echo and how it affects the measurement accuracy at the micron level.

### References for Section 17

- [17-1] R.C. Cook, R. McEachern, R.B. Stephens, *Fusion Technol.* **35**, P224 (1999).
- [17-2] R.B. Stephens, S.W. Hann, D.C. Wilson, "Characterization Specifications for Baseline Indirect Drive NIF Targets," presented at the 14th Target Fabrication Meeting, July 15–19, 2001 West Point, New York and to be published in *Fusion Technol.*
- [17-3] S.W. Haan, P.A. Amendt, T.R. Dittrich, et al., *Fusion Sci. Technol.* **45**, 69 (2004).
- [17-4] R.B. Stephens, D. Olson, H. Huang, J.B. Gibson, *Fusion Sci. Technol.* **45**, 210 (2004).
- [17-5] P. Subramanian, A. Zebib, B. McQuillan, *Phys. Fluids* **17**, 017103 (2005).
- [17-6] B.W. McQuillan, M. Takagi, *Fusion Sci. Technol.* **41**, 209 (2002).



## 18. 04PR01 PRECISION RADIOGRAPH (R. STEPHENS)

A key characteristic of beryllium shells employed for inertial fusion is the uniformity of their x-ray opacity; measurements required to validate a shell's acceptance call for extreme accuracy ( $1:10^4$ ) together with high spatial resolution (up to mode 200 on a 2 mm diameter shell). GA has undertaken to construct and demonstrate a precision radiograph suitable for the evaluation of fluctuations in the x-ray opacity of 2 mm diameter NIF shells. This system will contain a single-channel that can evaluate a swath covering about half the shell in 1-2 h.

The proposed approach is to use a single-channel system to measure a 50-100  $\mu\text{m}$  square area, repeatedly traversing the measurement area over the surface of a rotating, translating shell. This approach interleaves the measurements so that each is spread out over the whole measurement time, minimizing errors in the relative measurement. As a result, the relative uncertainty in these measurements should be dominated by the shot noise. Initial estimates were that  $10^8$  counts/pixel and  $\sim 10$  h would be sufficient to characterize a shell with  $\sim 50$   $\mu\text{m}$  spatial resolution.

The first year's milestone on this task was to demonstrate the capability to make opacity measurements with an accuracy of 1 part in  $10^4$ . Transmission was measured through a 200  $\mu\text{m}$  thick Be:Cu slab (0.9 at% Cu), with 0.2  $\mu\text{m}$  rms surface finish. It was mounted on a galvanometer shaft that could orient the slab with a relative uncertainty of  $\pm 10$   $\mu\text{radian}$ ; a rotation  $\sim 0.8$  deg changes the x-ray path length by  $1:10^4$ . The foil was mounted  $\sim 600$   $\mu\text{m}$  from the axis of rotation so the rotation is accompanied by a lateral shift of  $\sim 10$   $\mu\text{m}$  per degree of rotation. The x-ray tube had a Cr anode and filter. The Cr- $K_\alpha$  (5.4 keV) output was calculated to have  $\sim 60\%$  transmission. At that energy, the sensitivity to opacity or thickness changes,

$$\alpha = \partial \ln(\text{counts}) / \partial \ln(\text{thickness}) \sim 0.47 \quad . \quad (18-1)$$

The detected counts are the results of a large number of uncorrelated events, each of which has an associated uncertainty. A simple estimate, adding the uncertainties in quadrature, gives a shot noise about twice expected from the raw photomultiplier count

$$\sigma \sim 2 / \sqrt{\text{counts}} \quad . \quad (18-2)$$

Data was collected in 300 ms intervals with 35 ms intervals to allow galvanometer rotation and settling, and computer overhead. The count rate observed through a 57  $\mu\text{m}$  aperture was  $3 \times 10^5 \text{ s}^{-1}$ , considerably less than the maximum photomultiplier count rate ( $\sim 10^7 \text{ s}^{-1}$ ), so the aperture was enlarged to 430  $\mu\text{m}$ . The sample was stepped through the selected angles at each measurement interval, and the total at each angle was summed at the end of the run. The resulting data was fit to

$$I_{\text{fit}} = I_0 e^{-\frac{\alpha}{\cos(\theta - \theta_0)}} \quad , \quad (18-3)$$

where  $I_0$ ,  $\theta_0$ , and  $\alpha$  are fit parameters [Fig. 18-1(a)]. The data is for a run that collected  $10^8$  counts at 2 deg intervals over  $\pm 20$  deg. The curve is slightly asymmetrical because of a slight offset ( $\theta_0 = -2.36$  deg) in insertion of the cylindrical galvanometer housing. The sensitivity of these counts to thickness is  $\alpha_{\text{fit}} = 0.39$ , just about as calculated. Differences between the data and fit (shown as yellow triangles) show a spread  $\sigma$  ( $10^8$ )  $\sim 2 \times 10^{-4}$ , again about as calculated.

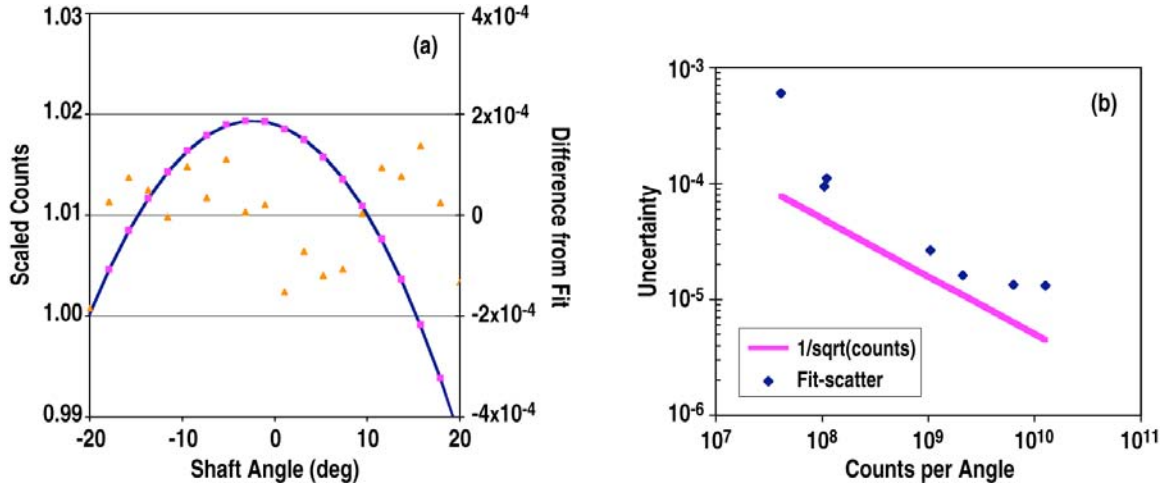


Fig. 18-1. (a) Scaled counts as a function of shaft angle (pink squares) fit to Eq. (18-3) (blue line). The differences from the fit are shown as orange triangles. (b)  $\sigma$  of deviation of experimental data from fits using Eq. (18-3) as a function of the number of counts per angle.

The dependence of uncertainty on counts was explored using data sets with successively increasing counts per pixel [Fig. 18-1(b)]. It is apparent that  $\sigma(N)$  approaches a floor of  $\sim 10^{-5}$  for  $N > 10^9$ . Comparison of fit deviations for the two runs with  $N \geq 10^{10}$  (Fig. 18-2) show that the deviation is systematic. We suspect that it arises from the transverse motion coupled to the rotation. The measured area shifts by  $\sim 1\%$  of its width between each angle ( $\Delta\theta = 0.4$  deg), resulting in a transmission fluctuation  $\sim 10^{-5}$ . That suggests a variability in thickness or opacity of  $\sim 10^{-3}$  averaged over scale lengths of  $\sim 400 \mu\text{m}$ . That is about the reported rms roughness of the sample.

We conclude from the above results that  $10^9$  counts/pixel is necessary to give a  $1-\sigma$  uncertainty in opacity  $\sim 10^{-4}$ . That results in a rather large shell measurement time. An alternative design uses a parallel line of 10 close-packed optical fibers arranged along the rotation axis to collect ten sets of data at once. This allows measurement in a reasonable time and eliminates the need to translate the shell along its rotation axis (simplifying construction). Detailed plans for this device will be developed by end of the first quarter and it should be operational by the end of FY05.

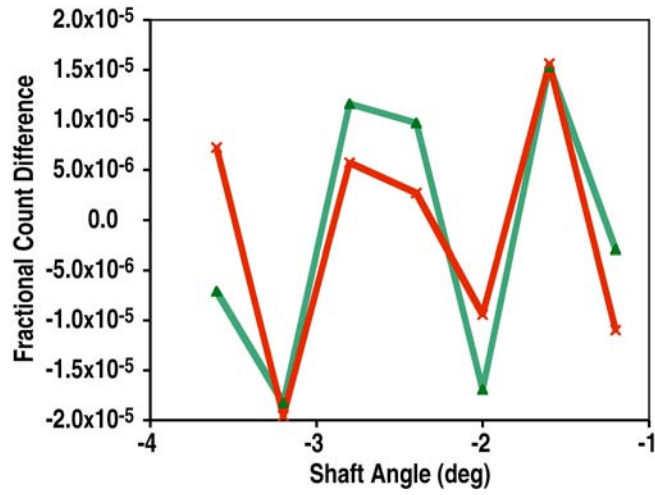


Fig. 18-2. Deviation from fit for the two runs with more than  $10^{10}$  counts/angle.

For further information contact Richard B. Stephens



## 19. 04SL03 BERYLLIUM SHELLS FOR SNL (A. NIKROO)

The goal of this task was to evaluate the possibility of fabrication of gas-filled beryllium shells for shots on SNL's Z machine, possibly in FY05. To produce such targets, we needed to address the fabrication of beryllium shells, the filling of the shells with gas, and ensuring the retention of the fill.

Since sputter coating of CH mandrels with beryllium has proven to be a practical way of producing beryllium shells, we decided to establish such coating at GA. However, given the safety related issues with beryllium, we decided to use the beryllium certified PISCES-II facility at UC San Diego to do this as quickly and efficiently as possible. This facility was located conveniently close to GA and our collaborative agreement with UCSD allowed the operation of the coater by GA personnel at UCSD. A properly ventilated, limited access enclosure within this facility provided the space for the GA coater. The coater parts were purchased using GA funds and assembled at UCSD outside the beryllium enclosure and commissioned using aluminum as a surrogate. The coater was then moved into the beryllium enclosure, with the control unit remaining outside the enclosure to allow easy access to the controls. Beryllium was deposited using this coater at UCSD in September, producing the first beryllium coated CH shells at GA. Since then CH mandrels have been coated at a variety of thicknesses. Figure 19-1(a) shows an electron microscope image of a  $50\ \mu\text{m}$  layer and Fig. 19-1(b) shows an x-ray image of  $\sim 17\ \mu\text{m}$  Be layer deposited on a  $\sim 20\text{-}30\ \mu\text{m}$  CH mandrel.

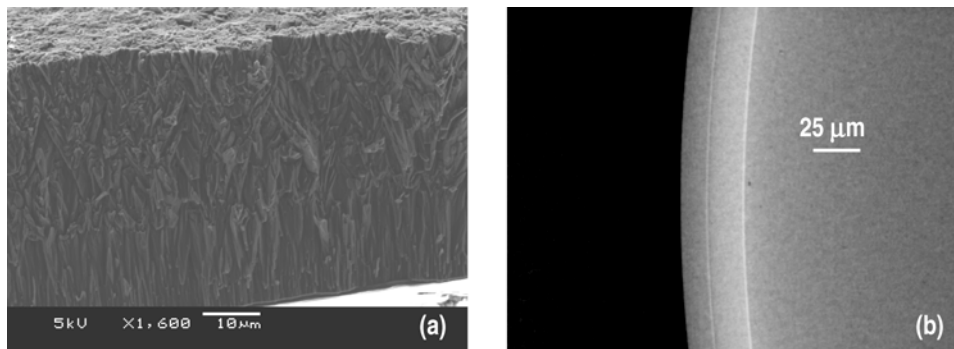


Fig. 19-1. (a) SEM image of a  $\sim 50\ \mu\text{m}$  Be layer microstructure change with deposition rate. (b) Radiograph of  $\sim 17\ \mu\text{m}$  Be layer on  $23\ \mu\text{m}$  CH mandrel.

Since the research at LLNL and LANL indicated that beryllium is practically impermeable to deuterium, filling the shells presents a special challenge. The accepted way of filling beryllium shells is to fill the shells through a hole drilled into the wall and then subsequently seal the hole. Therefore, in parallel with the coating effort, we designed and built a prototype fill chamber to allow sealing of the hole under the desired pressure of deuterium. The fill chamber is fitted with micromanipulators which can deliver a small amount of glue to seal the hole under as much as 500 psi of pressure (Fig. 19-2). This chamber was successfully tested using CH shells as surrogates. A  $\sim 50\ \mu\text{m}$  hole was drilled

into the CH mandrel by an Excimer laser and then sealed under 500 psi of deuterium (see Fig. 19-3). Proper sealing of the hole was verified by following the out permeation of the deuterium fill from the shell from the mass spectrometer signal obtained from the CH shell (Fig. 19-4). This signal resembled that expected from an intact shell (half-life of ~7 minutes). Extension of this technique to beryllium shells should be straightforward.



Fig. 19-2. Pressure cell with orthogonal optical access.

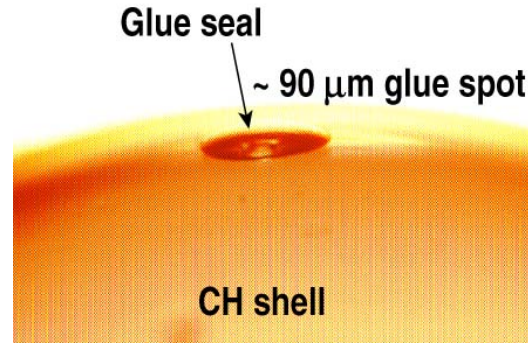


Fig. 19-3. Excimer laser drilled hole in CH mandrel.

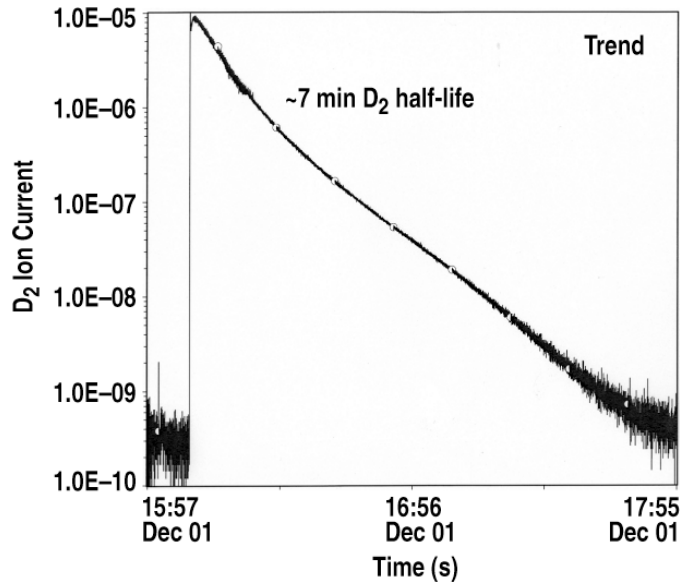


Fig. 19-4. Dycor System 200. DT-filled GDP shell: 2 mm o.d., 500 psi, hole plugged with ultraviolet (UV) glue.

Drilling of the hole remains a challenge for us for two reasons. Firstly, this process is still under development at LLNL and a femtosecond laser may be required. However, as the hole needed for the Z shots can be larger, a longer pulse laser can be used. Commercial outfits such as Exitech, which we have used in our polymer development work, can drill such holes using their lasers. However, the safety related issues with beryllium prevents them from

drilling the holes in beryllium shells. To bypass hole drilling directly into beryllium, we have begun exploring the possibility of producing a hole in the beryllium layer by coating a laser drilled CH mandrel. CH mandrels can be routinely drilled using Excimer lasers without any contamination issues. Initial results from coating such mandrels indicate that the hole remains open up to thicknesses of  $\sim 30 \mu\text{m}$  (see Fig. 19-5), but is closed by the coating at  $\sim 50 \mu\text{m}$  thickness. These are preliminary results and the hole closure process may be dependent on the coating conditions and needs to be explored further.

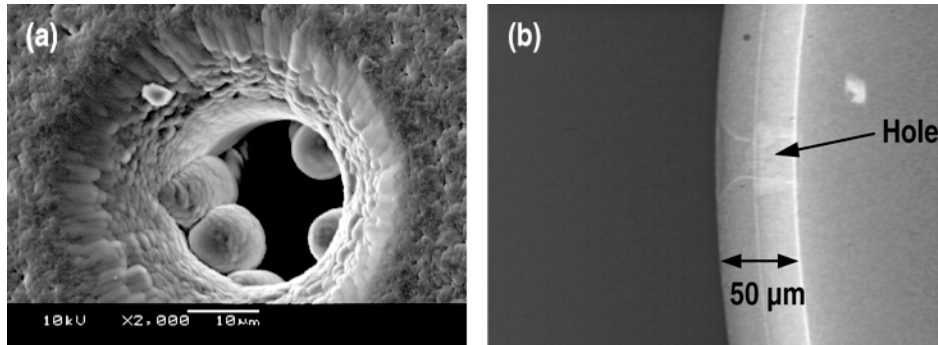


Fig. 19-5. Hole drilled in CH mandrel is duplicated in Be coating. (a) SEM image showing that the hole is indeed open at the top. (b) radiographic image again confirming that the hole is open through the Be and CH layers.



## 20. 04EQU-1 HIGH PRECISION MILLING MACHINE (J. KAAE)

This capital equipment task was used to purchase a compact high-precision milling machine. The machine selected was a Kern machine, which has five axes of motion. It is currently used to produce witness plates, shields, and metal and polymer components requiring precisely drilled holes and slots (Fig. 20-1).

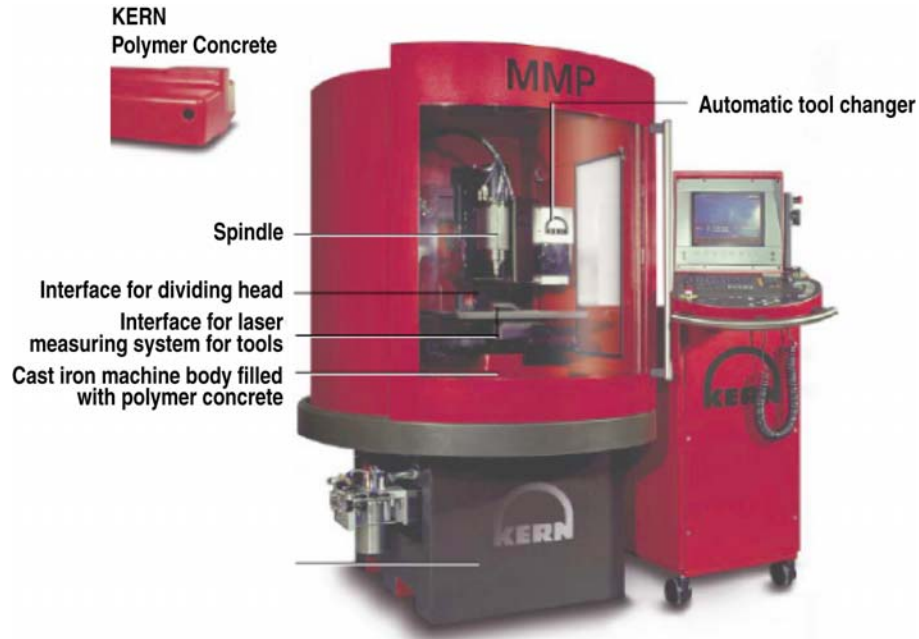


Fig. 20-1. Kern high-precision milling machine.



## 21. 04EQU-2 PURCHASE AND ASSEMBLE FILM MAPPING SYSTEM (K. SHILLITO)

Task Leader: Keith Shillito

Target Fabrication

During GFY04 Schafer Corporation purchased a Filmetrics Film Mapper for automated measurement of film thickness of our cast polyimide films. The Filmetrics F50 Film Mapper provides an automated method to measure a large area film on a silicon wafer. The equipment can quickly measure thickness, optical constants and roughness for thin film coatings. The Film Mapper uses a programmable motorized stage to provide up to 300 measured points per map. This provides consistent and quick measurements and reduces the amount of manpower necessary to characterize the requested targets (Fig. 21-1).

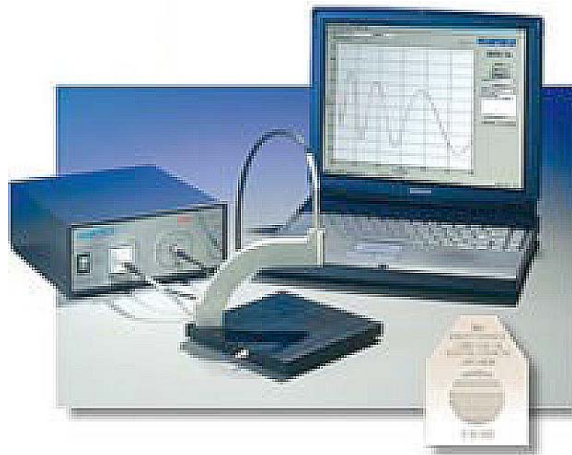


Fig. 21-1. Filmetrics F50 Film Mapper.



## 22. 04EQU-3 DIAMOND TURNING MACHINE (J. KAAE)

A compact three-axis ultra precision diamond turning machine was purchased with this capital equipment task. The machine selected was a Nanotech 220UPL-HD machine. It has slow tool servo capability, which means that complex three-dimensional surfaces can be produced, although there is a limit to the scale of the detail that can be cut. It is currently used to produce fast-ignition targets as well as hohlraums, witness plates, cones and other target components (Fig. 22-1).



Fig. 22-1. Nanotech 220UPL-HD diamond turning machine.



## 23. 04EQU-4 SURFACE PROFILER (K. SHILLITO)

Task Leader: Keith Shillito

During GFY04 Schafer Corporation purchased an Ambios XP-2 profilometer to replace an aging Tencor machine. The new profilometer gives us much greater capability than the old one in stylus selection, force adjustment, plotting and measurement options, and analysis capability. The Ambios profiler has a software-adjustable force on the stylus that can be as light as 0.05 mg. This allows us to characterize surfaces that are softer without damaging them or to use a much smaller radius stylus, as small as  $2.5 \mu\text{m}$ , to measure more complex surface features. The Ambios profiler provides for easy stylus replacement so we can choose the best radius and shape for each job. We have used the profiler to measure sine wave patterns on polystyrene, finish and features on machined aluminum components, and to cross check thickness measurements and step height measurements made with other profilometers. In addition to the standard trace capability, the Ambios profiler can be programmed to make several parallel traces. Software then combines the traces to generate a 3D surface that can be analyzed or displayed in reports. The Ambios software has a wide variety of data analysis routines including step height and wavelength analysis, FFT, and several types of roughness analysis. Data can also be exported to other programs such as Excel or MathCAD for custom analysis. An image of the XP-2 and a sample on the stage is shown in Fig. 23-1.

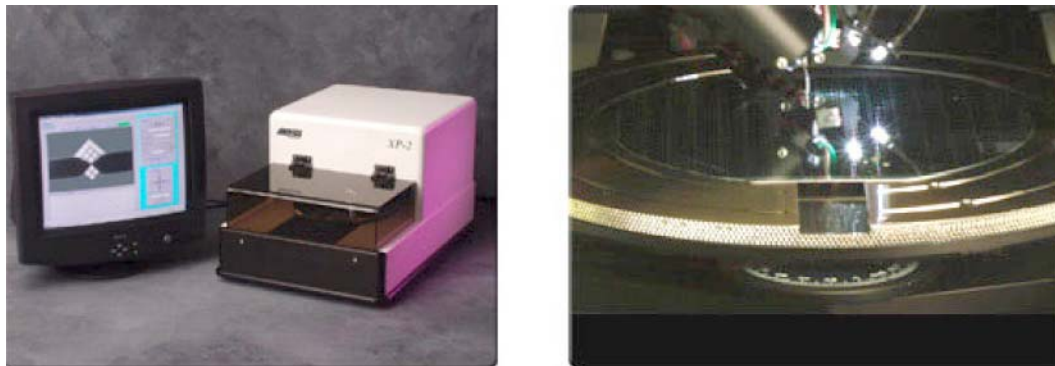


Fig. 23-1. Ambios XP-2 profilometer.



## 24. 04EQU-5 AUTOMATED INSPECTION MICROSCOPE (K. SHILLITO)

Task Leader: Keith Shillito

During GFY04 Schafer Corporation purchased a Nikon NEXIV VMR 3020 Video Measuring System. This system greatly facilitates the characterization of target components by virtue of programmable software that allows automated operation when measuring many parts. It offers a variety of illumination choices that facilitate accurate detection of edges in molded parts and provides long working distances (50 mm) that permit measurements of parts with big height gaps. A 15X zoom provides universal applications while facilitating easy search at low magnifications and accurate measurements at high magnifications while employing user-friendly software. The laser Auto Focus facilitates evaluations of cross-sectional shapes and 3D profiling as well as the flatness of work-piece surfaces. An image of this system is shown in Fig. 24-1.



Fig. 24-1. A Nikon NEXIV VMR 3020 Video Measuring System.



## 25. PUBLICATIONS

Items with GA/Schafer efforts supported by the contract for Target Component Fabrication and Technology Development Support are marked with an asterisk.

Frey, D.T., D.T. Goodin, R.W. Stemke, R.W. Petzoldt, T.J. Drake, W. Egli, B.A. Vermillion, R. Klasen, M.M. Cleary, “REP-Rated Target Injection for Inertial Fusion Energy,” Proc. 16th ANS Top. Mtg. on Technology of Fusion Energy, September 14–16, 2004, Madison, Wisconsin, to be published in Fusion Sci. Technol.; General Atomics Report GA–A24820 (2004).

Giraldez, E., and J.L. Kaae, “Fabrication of Window Saddles for NIF Cryogenic Hohlräume,” presented at the 15th Target Fabrication Specialists Meeting, June 1–5, 2003, Glendon Beach, Oregon, Fusion Sci. Technol. **45**, 206 (2004); General Atomics Report GA–A24505 (2003).

Goodin, D.T., A. Nobile, N.B. Alexander, R. Gallix, J.L. Maxwell, R.W. Petzoldt, W.S. Rickman, E.I. Valmianski, “Progress in Heavy Ion Driven Target Fabrication and Injection,” presented at the 15th Intl. Symp. on Heavy Ion Inertial Fusion, June 7–11, 2004, Princeton, New Jersey and to be published in Nucl. Instr. and Methods in Physics Research A; General Atomics Report GA–A24727 (2004).

Goodin, D.T., N.B. Alexander, L.C. Brown, D.A. Callahan, P. Ebey, D.T. Frey, R. Gallix, D. Geller, C.R. Gibson, J. Hoffer, J.L. Maxwell, B.W. McQuillan, A. Nikroo, A. Nobile, C. Olson, R.W. Petzoldt, R. Raffray, W.S. Rickman, G. Rochau, D.G. Schroen, J. Sethian, J. Sheliak, J.E. Streit, M. Tillack, B.A. Vermillion, And E.I. Valmianski, “Demonstrating a Target Supply for Inertial Fusion Energy,” Proc. 16th ANS Top. Mtg. on Technology of Fusion Energy, September 14–16, 2004, Madison, Wisconsin, to be published in Fusion Sci. Technol.; General Atomics Report GA–A24816 (2004).

Goodin, D.T., A. Nobile, D.G. Schroen, J.L. Maxwell, and W.S. Rickman, “Cost-Effective Target Fabrication for Inertial Fusion Energy,” 3rd Int. Conf. on Inertial Fusion Sciences and Applications, September 7–12, 2003, Monterey, California, in Inertial Fusion Sciences and Applications 2003, eds. B.A. Hammel, D.D. Meyerhofer, J. Meyer-ter-Vehn, and H. Azechi (American Nuclear Society, 2004) pp. 753-757; General Atomics Report GA–A24429 (2003).

Goodin, D.T., N. Alexander, L. Brown, D. Frey, R. Gallix, C. Gibson, J. Maxwell, A. Nobile, R. Petzoldt, R. Raffray, G. Rochau, D. Schroen, M. Tillack, W. Rickman, B. Vermillion, “A Cost-Effective Target Supply for Inertial Fusion Energy,” Nucl. Fusion **44**, 254 (2004); General Atomics Report GA–A24667 (2004).

- Hill, D.W., E. Castillo, K.C. Chen, S.E. Grant, A.L. Greenwood, J.L. Kaae, A. Nikroo, S.P. Paguio, C. Shearer, J.N. Smith, Jr., R.B. Stephens, D.A. Steinman, J. Wall, "Fabrication and Characterization of Fast Ignition Targets," presented at the 15th Target Fabrication Specialists Meeting, June 1–5, 2003, Gleneden Beach, Oregon, Fusion Sci. Technol. **45**, 113 (2004); General Atomics Report GA–A24443 (2003).
- Huang, H., R.B. Stephens, D.W. Hill, C. Lyon, A. Nikroo, D.A. Steinman, "Automated Batch Characterization of ICF Shells with Vision-Enabled Optical Microscope System," presented at the 15th Target Fabrication Specialists Meeting, June 1–5, 2003, Gleneden Beach, Oregon, Fusion Sci. Technol. **45**, 214 (2004); General Atomics Report GA–A24442 (2003).
- McQuillan, B.W., R. Paguio, P. Subramanian, M. Takagi, A. Zebib, "Hydrodynamic Issues in PAMS Mandrel Target Fabrication," 3rd Int. Conf. on Inertial Fusion Sciences and Applications, September 7–12, 2003, Monterey, California, in Inertial Fusion Sciences and Applications 2003, eds. B.A. Hammel, D.D. Meyerhofer, J. Meyer-ter-Vehn, and H. Azechi (American Nuclear Society, 2004) pp. 766-769; General Atomics Report GA–A24438 (2004).
- Nikroo, A., J. Pontelandolfo, A.L. Greenwood, J.L. Stillwell, D.A. Callahan, "Fabrication of Capsules with an Angle Dependent Gold Shim for Hoholraum Drive Symmetry Correction," presented at the 15th Intl. Symp. on Heavy Ion Inertial Fusion, June 7–11, 2004, Princeton, New Jersey, to be published in Nucl. Instr. and Methods in Physics Research A; General Atomics Report GA–A24774 (2004).
- Nikroo, A., D. Czechowicz, R. Paguio, A.L. Greenwood, M. Takagi, "Fabrication and Properties of Overcoated Resorcinol-Formaldehyde Shells for OMEGA Experiments," presented at the 15th Target Fabrication Specialists Meeting, June 1–5, 2003, Gleneden Beach, Oregon, Fusion Sci. Technol. **45**, 84 (2004); General Atomics Report GA–A24451 (2003).
- Nikroo, A., E. Castillo, D.W. Hill, A.L. Greenwood, "Preparation of Cu-Doped Glow Discharge Polymer Coatings for ICF Applications," presented at the 15th Target Fabrication Specialists Meeting, June 1–5, 2003, Gleneden Beach, Oregon, Fusion Sci. Technol. **45**, 144 (2004); General Atomics Report GA–A24453 (2003).
- Nikroo, A., D. Czechowicz, K.C. Chen, M. Dicken, C. Morris, R. Andrews, A.L. Greenwood, E. Castillo, "Mechanical Properties of Thin GDP Shells Used as Cryogenic Direct Drive Targets at OMEGA," presented at the 15th Target Fabrication Specialists Meeting, June 1–5, 2003, Gleneden Beach, Oregon, Fusion Sci. Technol. **45**, 229 (2004); General Atomics Report GA–A24457 (2003).
- Nikroo, A., W. Baugh, and D.A. Steinman, "Fabrication of Gas-Filled Tungsten-Coated Glass Shells," presented at the 15th Target Fabrication Specialists Meeting, June 1–5, 2003, Gleneden Beach, Oregon, Fusion Sci. Technol. **45**, 202 (2004); General Atomics Report GA–A24458 (2003).

- Nikroo, A., J. Bousquet, R. Cook, B.W. McQuillan, R. Paguio, M. Takagi, "Progress in 2 mm Glow Discharge Polymer Mandrel Development for NIF," presented at the 15th Target Fabrication Specialists Meeting, June 1–5, 2003, Gleneden Beach, Oregon, Fusion Sci. Technol. **45**, 165 (2004); General Atomics Report GA–A24483 (2003).
- Petzoldt, R.W., N.B. Alexander, T.J. Drake, D.T. Goodin, K. Jonestrack, R.W. Stemke, B.A. Vermillion, "Experimental Target Injection and Tracking System Construction and Single Shot Testing," 3rd Int. Conf. on Inertial Fusion Sciences and Applications, September 7–12, 2003, Monterey, California, in Inertial Fusion Sciences and Applications 2003, eds. B.A. Hammel, D.D. Meyerhofer, J. Meyer-ter-Vehn, and H. Azechi (American Nuclear Society, 2004) pp. 815-819; General Atomics Report GA–A24432 (2003).
- Petzoldt, R.W., K. Jonestrack, "IFE Target Injection Tracking and Position Prediction Update," Proc. 16th ANS Top. Mtg. on Technology of Fusion Energy, September 14–16, 2004, Madison, Wisconsin, to be published in Fusion Sci. Technol.; General Atomics Report GA–A24817 (2004).
- Project Staff, "Advanced Fusion Technology Research and Development, Annual Report to the U.S. Department of Energy, October 1, 2001 through September 30, 2002," General Atomics Report GA–A24304 (2003).
- Project Staff, "Target Injection, Tracking, Fabrication and Characterization Development in Support of the NRL Laser-Plasma Program Annual Report to the U.S. Department of Navy, March 6, 2003 through April 17, 2004," General Atomics Report GA–A24761 (2004).
- Rickman, W.S., D.T. Goodin, "Cost Modeling for Fabrication of IFE Targets," Proc. 2nd IAEA Tech. Mtg on Phys. and Tech. of Inertial Fusion Energy Targets and Chambers, San Diego, California, 2002, in Fusion Sci. Technol. **43**, 353 (2003); General Atomics Report GA–A24074 (2002).
- Steinman, D.A., R. Wallace, S.E. Grant, M.L. Hoppe, J.N. Smith, Jr., "Fabrication of a New Type of Double-Shell Target Having a PVA Inner Layer," presented at the 15th Target Fabrication Specialists Meeting, June 1–5, 2003, Gleneden Beach, Oregon, Fusion Sci. Technol. **45**, 124 (2004); General Atomics Report GA–A24455 (2003).
- Stephens, E.H., A. Nikroo, D.T. Goodin, R.W. Petzoldt, "Optimizing High Z Coatings for IFE Shells," Proc. 2nd IAEA Tech. Mtg. on Physics and Technology of Inertial Fusion Energy Targets and Chambers, San Diego, California, 2002, in Fusion Sci. Technol. **43**, 456 (2003); General Atomics Report GA–A24057 (2002).

- Stephens, R.B., M.J. Bonino, S. Fujioka, S.P. Hatchett, D.W. Hill, A. Nikroo, T.C. Sangster, H. Shiraga, J.N. Smith, Jr., C. Stoeckl, K.A. Tanaka, "Hydrodynamics of Direct Drive Reentrant Cone Targets for Fast Ignition," 3rd Int. Conf. on Inertial Fusion Sciences and Applications, September 7–12, 2003, Monterey, California, in Inertial Fusion Sciences and Applications 2003, eds. B.A. Hammel, D.D. Meyerhofer, J. Meyer-ter-Vehn, and H. Azechi (American Nuclear Society, 2004) pp. 383-386; General Atomics Report GA-A24444 (2004).
- Stephens, R.B., "Implosion of Indirectly Driven Reentrant Cone Shell Target," Phys. Rev. Lett. **91**, 185001 (2003); General Atomics Report GA-A24244 (2003).
- Stephens, R.B., S.P. Hatchett, R. Turner, C. Stoeckl, J.A. Delettrez, T.C. Sangster, S. Fujioka, H. Shiraga, K.A. Tanaka, "Cone Dynamics in Fast Ignitor Cone Targets on OMEGA," Bull. Am. Phys. Soc. **48**, 298 (2003).
- Stephens, R.B., R.A. Snavely, Y. Aglitskiy, F. Amiranoff, C. Andersen, D. Batani, S.D. Baton, T. Cowan, R.R. Freeman, T. Hall, S.P. Hatchett, J.M. Hill, M.H. Key, J.A. King, J.A. Koch, M. Koenig, A.J. Mackinnon, K.L. Lancaster, E. Martinolli, P. Norreys, E. Perelli-Cippo, M. Rabec Le Gloahec, C. Rousseaux, J.J. Santos, And F. Scianitti, "K $\alpha$  Fluorescence Measurement of Relativistic Electron Transport in the Context of Fast Ignition," Phys. Rev. E **69**, 066414 (2004); General Atomics Report GA-A24325 (2003).
- Stephens, R.B., D. Olson, H. Huang, J.B. Gibson, "Complete Surface Mapping of ICF Shells," presented at the 15th Target Fabrication Specialists Meeting, June 1–5, 2003, Glendon Beach, Oregon, Fusion Sci. Technol. **45**, 210 (2004); General Atomics Report GA-A24452 (2003).
- Vermillion, B.A., G.E. Besenbruch, L.C. Brown, D.T. Goodin, B.W. McQuillan, M. Takagi, "Microencapsulation Studies for Mass Production of IFE Targets," 3rd Int. Conf. on Inertial Fusion Sciences and Applications, September 7–12, 2003, Monterey, California, in Inertial Fusion Sciences and Applications 2003, eds. B.A. Hammel, D.D. Meyerhofer, J. Meyer-ter-Vehn, and H. Azechi (American Nuclear Society, 2004) pp. 770-773; General Atomics Report GA-A24431 (2003).
- Vermillion, B.A., B.W. McQuillan, L.C. Brown, D.T. Goodin, R. Paguio, J.E. Streit, D.G. Schroen, P.C. Goodman, W. Maksiarekul, "Mass Production Methods for IFE Targets," Proc. 16th ANS Top. Mtg. on Technology of Fusion Energy, September 14–16, 2004, Madison, Wisconsin, to be published in Fusion Sci. Technol.; General Atomics Report GA-A24827 (2004).
- Whyte, D.G., T.E. Evans, C.P.C. Wong, W.P. West, R. Bastasz, J.P. Allain, J. Brooks, "Experimental Observations of Lithium as a Plasma-Facing Surface in the DIII-D Tokamak Divertor," Fusion Engin. Design **72**, 133 (2004); General Atomics Report GA-A24401 (2003).

Wong, C.P.C., S. Malang, M. Sawan, I. Sviatoslavsky, E. Mogahed, S. Smolentsev, S. Majumdar, B. Merrill, R. Mattas, M. Friend, J. Bolin, S. Sharafat, "APEX Advanced Ferritic Steel, FLiBE Self-Cooled First Wall and Blanket Design," Proc. 11th Intl. Conf. on Fusion Reactor Materials, December 7–12, 2003, Kyoto, Japan; General Atomics Report GA–A24520 (2003).



## **ACKNOWLEDGMENT**

This report of work was prepared for the U.S. Department of Energy under Contract No. DE-AC03-01SF22260.